Volume 9

# LLE Review
## Quarterly Report

October, 1981 - December, 1981
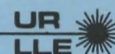
UR
LLE

# LLE Review

**Quarterly Report**

*Editor:* S. D. Jacobs
(716-275-4837)

October, 1981 - December, 1981

# IN BRIEF

This edition of the LLE Review contains articles on new developments in laser engineering, OMEGA experiments, plasma theory, and sub-picosecond research that occurred during the last quarter of 1981. Some of the highlights of the work described in this issue are the following:

- Optical absorption signatures from impurities in thin film dielectric coatings have been measured with photoacoustic absorption spectroscopy. This technique may prove useful for understanding and improving the damage thresholds of coatings employed in LLE laser systems.

- Preliminary results from target interaction experiments on OMEGA at long pulses confirm that the absorption mechanism changes from inverse bremsstrahlung to resonance absorption as laser intensity on target increases from $10^{14}\text{W/cm}^2$ to $10^{15}\text{W/cm}^2$.

- A theoretical analysis of filamentation of laser light entering a laser-plasma corona shows that plasma flow transverse to the filaments can significantly alter the thresholds and growth rates for this type of instability.

- An improved method for interpreting laser fusion target interferograms will provide the target fabrication group with a means for measuring small values of target shell nonconcentricity. It will be

possible to perform this measurement on gas-filled glass micro-balloons possessing a wide range of fill pressure.

• Modification to the chemical structure of polymer coatings used to form ablation layers on laser fusion targets reduces their crystalline texture. After annealing, these modified polymer coatings exhibit a smoother surface and more uniform density, two desirable target features for uniform laser-driven implosions.

• The monoenergetic photoelectron replica of an optical pulse that is produced by the image converter tube in a streak camera can be used to study laser-induced structural changes in materials in the picosecond time domain. Transmission electron diffraction patterns of an aluminum specimen 150 Å thick have been obtained with a single 100 psec electron pulse.

• Laser pulses shorter than 70 femtoseconds have been generated in a dye laser synchronously pumped by a frequency-doubled CW mode-locked Nd:YAG laser. These short pulsewidths are obtained at a wavelength of 615 nm with an overall efficiency of 10%.

# CONTENTS

*Bill Watson, lead mechanical engineer in the experimental area, preparing the copper activation counter, one of many OMEGA target diagnostics, prior to a 24-beam OMEGA system shot.*

# Section 1
# LASER SYSTEM REPORT

## 1.A GDL Facility Report

GDL continued operations as a 0.35$\mu$m irradiation facility during the first quarter of FY82.

A total of 670 shots were delivered by the facility in the November 1 to December 31, 1981 period. The shot distribution was as follows:

| | | |
|---|---|---|
| 3$\omega$ Target Experiments | 208 | Shots |
| X-Ray Program | 95 | |
| Damage Test Facility | 301 | |
| Alignment | 66 | |
| TOTAL | 670 | Shots |

During this period the first series of experiments with a 1nsec pulse-width was conducted. Initial measurements included stimulated Raman scattering and continuum x-ray spectroscopy. During this quarter the first series of experiments on kinetic x-ray diffraction was successfully completed and will be discussed in a future issue of the LLE Review.

# 1.B OMEGA Facility Report

Most of the final quarter of 1981 was spent installing a new one-nanosecond active-passive mode-locked oscillator in the OMEGA driver line.

The new oscillator required an additional optical table, oscillator PFN reconfiguration, and numerous cable and timing changes associated with its longer cavity round trip time of 18.3 nanoseconds (compared to 10.0 nanoseconds for the short-pulse cavity). The beam waist is different as well; this required that we adjust the fill factor with hard aperture and air spatial filter pinhole changes.

Anticipating the driver line restaging that will have to be carried out when the Kuizenga oscillator is incorporated into the OMEGA driver in 1982, we made detailed measurements of the whole-beam energy and near-field beam profile at all significant driver locations. These were used to normalize the energy code, RAINBOW, and to identify any component degradation since the last series of measurements.

With respect to degradation we found that there was very little, if any, permanent change in the driver gains and losses. Realignment of several of the dielectric polarizers in the Pockels cell and Faraday rotator assemblies restored the initially low driver output to design level.

Figure 1 shows the key measurement positions, and Table 1 tabulates the energies measured at these points.

*Fig. 1*
*Staging configuration in the OMEGA driver line. Numbers 1 through 8 indicate positions where beam energy at maximum output was measured for 1 nsec oscillator pulses.*



G1047
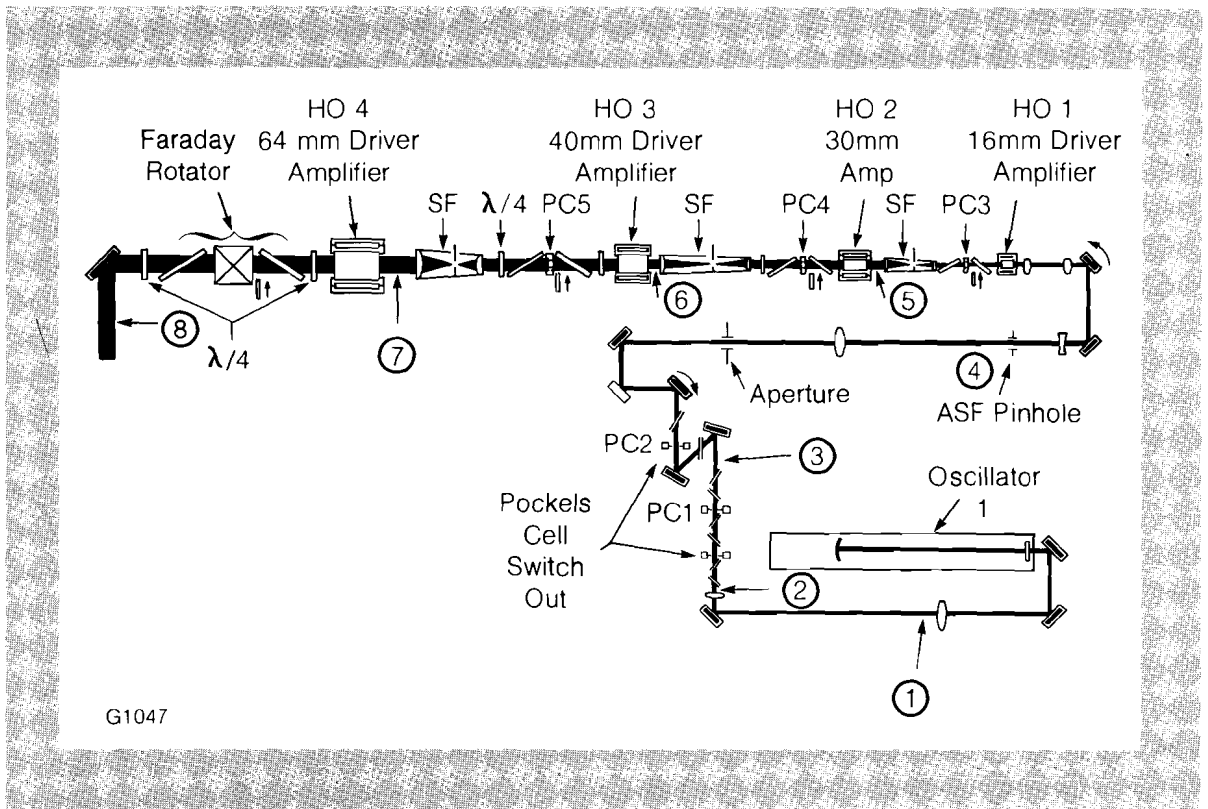
| Key | Calorimeter Location | Unamplified Train Energy, $\mu$J | Unamplified Single-Pulse Energy, $\mu$J | Amplified Single-Pulse Energy, J |
|-----|---------------------|----------------------------------|------------------------------------------|----------------------------------|
| 1 | After Collimating Lens | 10,000 | ~ 500 (est.) | — |
| 2 | Input to PC 1 | 8,400 | ~ 400 (est.) | — |
| 3 | Input to PC 2 | 4,400 | 200 | — |
| 4 | After Air Spatial Filter Pinhole | 1,800 | 80 | — |
| 5 | At HO 2 Input | 1,250 | 40 - 50 | 0.0044 |
| 6 | At HO 3 Input | 550 | 20 - 30 | 0.08 - 0.10 |
| 7 | At HO 4 Input | 480 | ~ 20 | 1.88 |
| 8 | Driver Output | 330 | ~ 15 | 16.40 |

G1056

*Table 1*
*OMEGA driver baseline energy at maximum output with 1 nsec oscillator pulses (November, 1981).*

The distribution of OMEGA system shots during this period was as follows:

| | |
|---|---|
| Target Shots | 38 |
| OMEGA Test Shots | 78 |
| Driver Line Test Shots | 117 |
| Software Test Shots | 131 |
| **TOTAL** | **364** |

# 1.C Photoacoustic Absorption Spectroscopy for Defect Analysis in Thin Films

Laser-induced damage to optical thin film coatings is the fundamental limitation in the design and construction of large laser systems used to investigate the feasibility of energy generation through thermonuclear fusion. Recent work by several groups has suggested that this damage is caused by the presence of defects on the order of one micron in dimension located in the thin film or at the film-substrate interface.[1,2] Impurities are one type of defect, but another type might be non-stoichiometric regions of the coating. In an attempt to establish more clearly the existence of these defects, and their relationship to laser-induced damage, we have begun to examine numerous optical micro-analytical techniques. In this article we discuss the use of photo-acoustic absorption spectroscopy (PAS) to locate absorbing defects in dielectric thin films.

In PAS a laser beam is focussed onto a thin film-coated substrate contained within a specially designed cell. The portion of the coating being irradiated will heat if it contains an impurity that absorbs at the laser

3

wavelength. The air confined to the cell and adjacent to the coating will also experience a temperature rise as heat flows to it from the impurity. By mechanically chopping the laser beam a periodic pressure wave is produced which can be detected by a microphone built into the photo-acoustic absorption cell. The magnitude of the acoustic signal detected correlates well with the absorption strength of the impurities in the coating.

PAS offers a versatility not found in other techniques like laser calorimetry. With highly sensitive microphones, phase-locked electronic processing technology, and tightly focussed laser beams, PAS is capable of detecting absorbing sites a few microns in diameter possessing absorption coefficients of $10^{-4}cm^{-1}$. By scanning the laser across the coated part or moving the part under the focussed beam, a two-dimensional map showing the sizes and locations (clustering) of impurities can be generated. By varying the laser wavelength, a photoacoustic spectrum that faithfully replicates an optical absorption spectrum can be obtained that might ultimately make impurity identification possible. The single most severe limitation to the use of PAS is its sensitivity to acoustic noise. Care must be taken to locate PAS experiments in a relatively noise-free environment, and to employ laboratory equipment (lasers, mechanical choppers, stepper motors) that generate little acoustic noise.
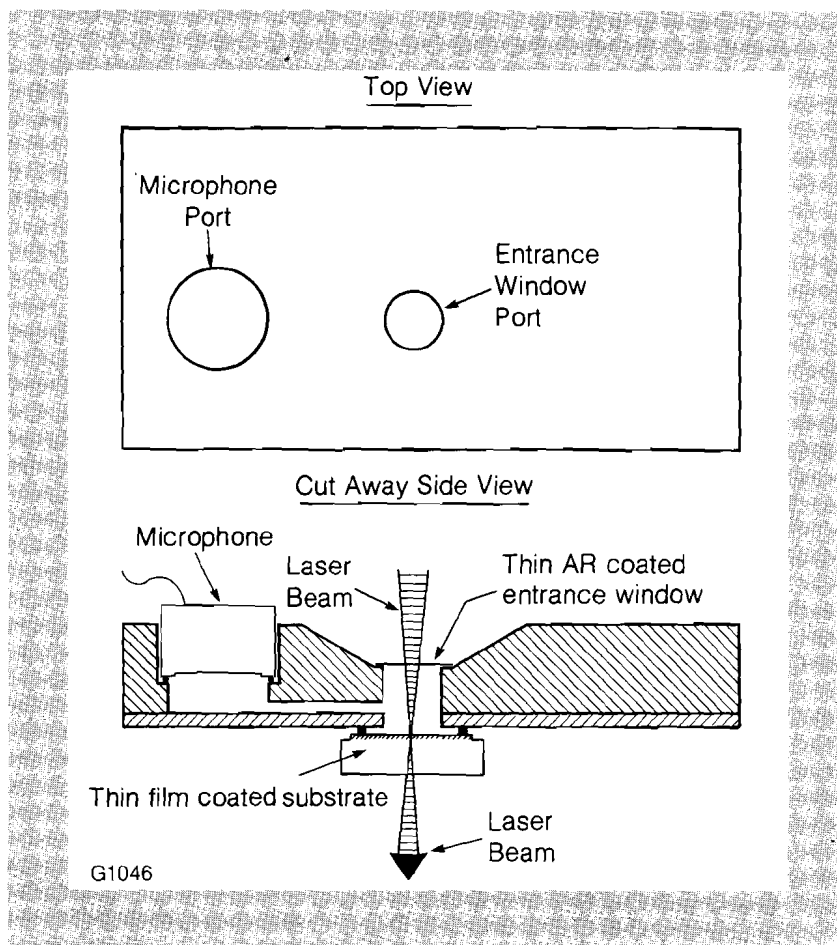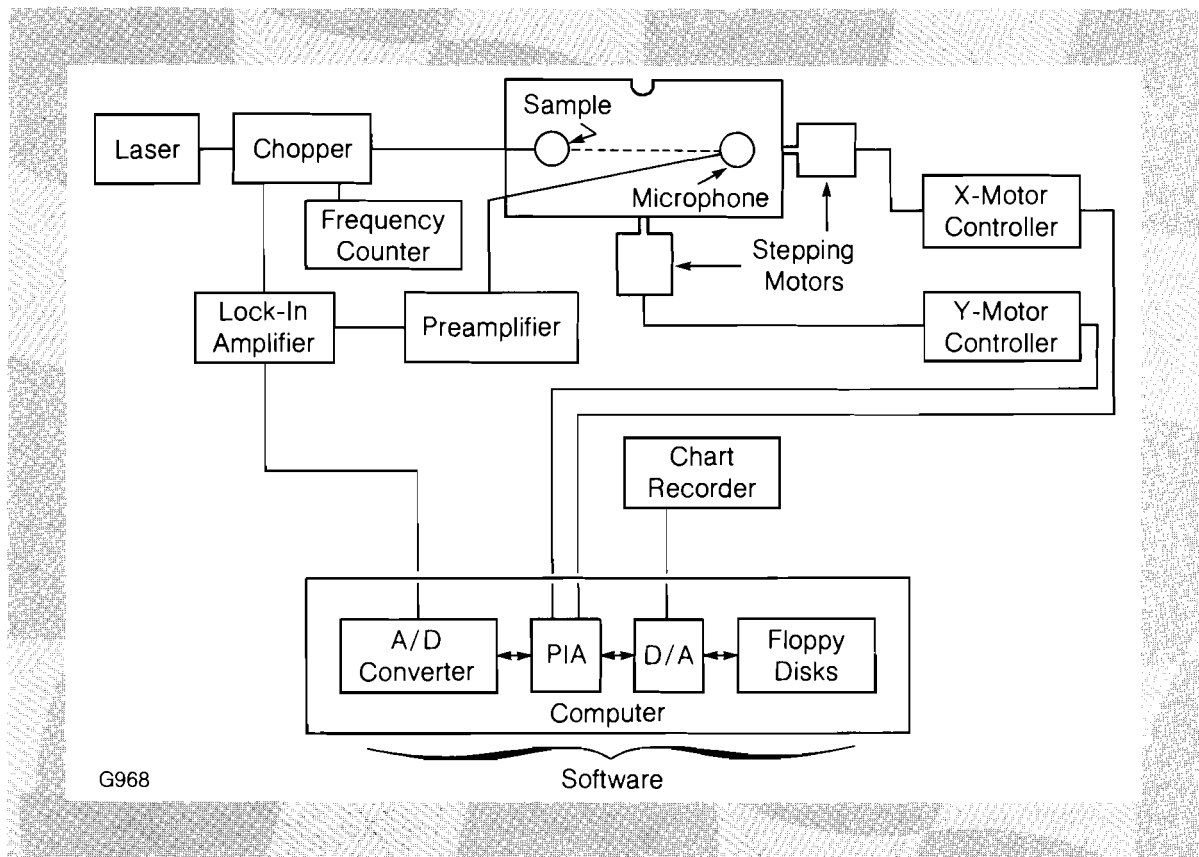


Fig. 2
Design of photoacoustic absorption cell. The distance between the entrance window and coated substrate surface (2mm), and the diameter of the narrow passage between the sample air chamber and the microphone air chamber (1.5mm) are minimized to enhance the signal-to-noise ratio of the cell. The microphone is a Buel and Kjaer model 4144 (25mm diameter) with a 100 Å thick diaphragm.

Experiments using PAS at Rochester started in the late 1970's with lasers operating in the infrared at wavelengths of 10,600 nm and 1060 nm and with focal spot sizes between 100 and 200 microns in diameter.[3,4] Work described here uses a Coherent Radiation CR6 argon ion laser operating at any one of several selectable wavelengths in the visible between 514.5 nm and 476.5 nm, a focussed spot size 6 to 8 microns in diameter, and a photoacoustic cell modified from a previous in-house design.[4] A schematic representation (not to scale) of the cell design is given in Fig. 2. A key to minimizing the cell's sensitivity to background acoustic noise is the reduced size of the air chambers above the sample, below the microphone and in the connecting passageway. Measurements on uniformly absorbing samples demonstrate that a laser-chopping frequency of 355 Hz gives the optimum signal-to-noise performance for this modified cell.

A block diagram of the components that comprise the photoacoustic absorption apparatus is given in Fig. 3. X-Y translation stages with stepping motors driven by commands from a minicomputer control the movement of the stage supporting the cell. Acoustic signals are preamplified and sensed by a lock-in amplifier referenced to the 355 Hz mechanically chopped frequency of the incident laser beam. The minicomputer stores lock-in amplifier data on floppy disks for off-line reprocessing, and also generates hard copy two-dimensional maps on a strip chart recorder. An attractive feature of the translation stages is that their absolute locations are displayed digitally on each controller. This provides an origin to which any scan may be referenced.

*Fig. 3*
*Block diagram of photoacoustic absorption apparatus. A Southwest Technical Products Corporation 6800 minicomputer with a Motorola 6800 microprocessor controls acquisition and storage of acoustic signals from a Princeton Applied Research model 124 lock-in amplifier. The computer also operates the translation stages, manufactured by Aerotech, Inc., to scan in raster fashion the coated parts beneath the laser beam.*



G968
Software

5

The ultimate resolution and sensitivity of this apparatus are demonstrated by the data shown in Fig. 4. By working with polystyrene balls from fifteen microns to one micron in diameter the minimum detectable ball size using a focussed laser beam eight microns in diameter was determined to be two microns. The photoacoustic signal generated by this barely resolvable ball corresponds to an absorption coefficient of $5 \times 10^{-4} cm^{-1}$.



With background noise          With noise statistically eliminated

G955
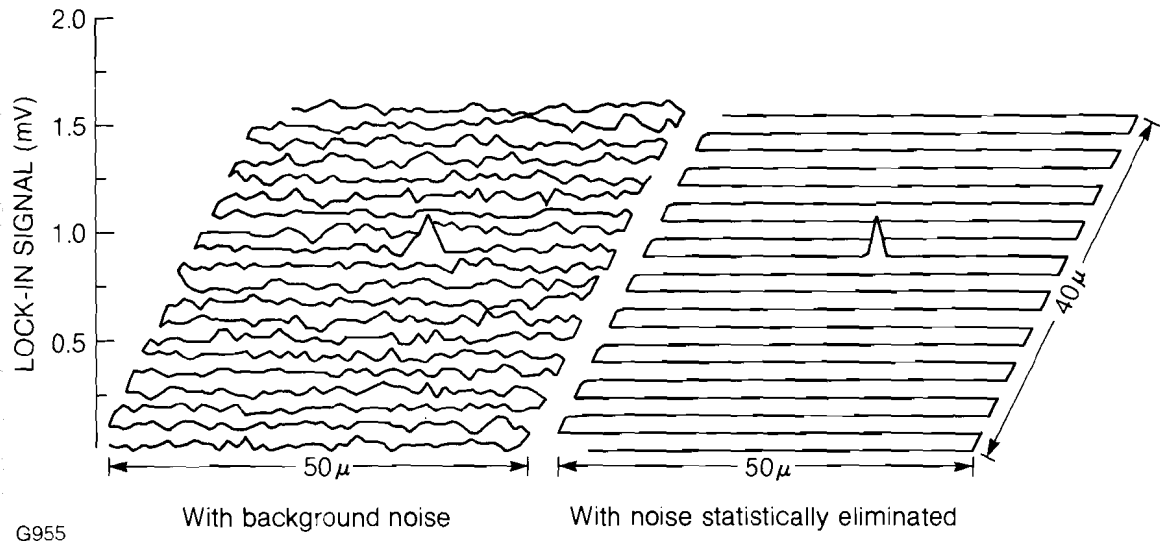
Fig. 4
Photoacoustic signals generated from a raster scan of a 2 micron diameter polystyrene ball on a bare glass surface. Computer-aided statistical analysis of stored data to eliminate background noise indicates that the apparatus can detect absorbing sites 2 microns in size. This scan was generated with the argon ion laser operating at a wavelength of 0.5145 microns with an output power of 150mW.

Fig. 5
Photoacoustic signal from carbon black. The response is in agreement with optical absorption data which shows carbon black to be a uniformly flat absorber in the blue-green region of the spectrum.

The spectral response of the photoacoustic absorption apparatus has been examined in two ways. Figure 5 shows the acoustic signal obtained from carbon black powder on a glass substrate support as a function of laser wavelength from 476.5 nm to 514.4 nm. Carbon black exhibits wavelength-independent absorption in the bluegreen spectral



G1002          WAVELENGTH (nm)

region,[6] and this is confirmed by the photoacoustic response. Figure 6 gives the acoustic signal from a sample of neodymium-doped glass that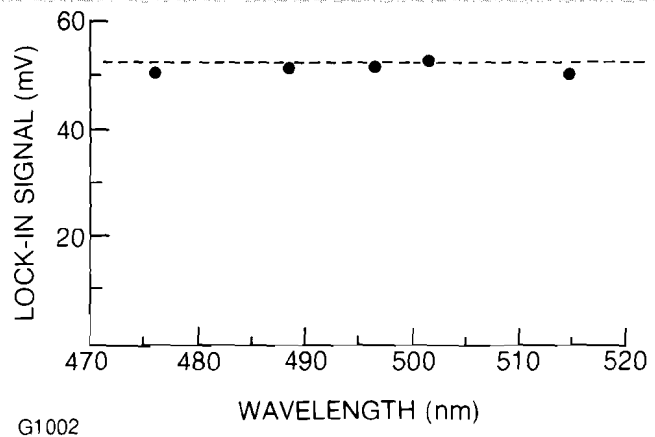 has been examined over the same wavelength range. The wavelength-dependent optical absorption signature of the $Nd^{+3}$ ions, as generated from spectrometer scans, is faithfully replicated by the photoacoustic signal.

*Fig. 6*
*Photoacoustic absorption signal compared to optical absorption for sample of neodymium-doped glass. The wavelength dispersion of optical absorption exhibited by the $Nd^{+3}$ ions is reproduced by the photoacoustic absorption signature after adjusting the acoustic signal scale so that the optical and acoustic data points coincide at a wavelength of 476.5 nm.*
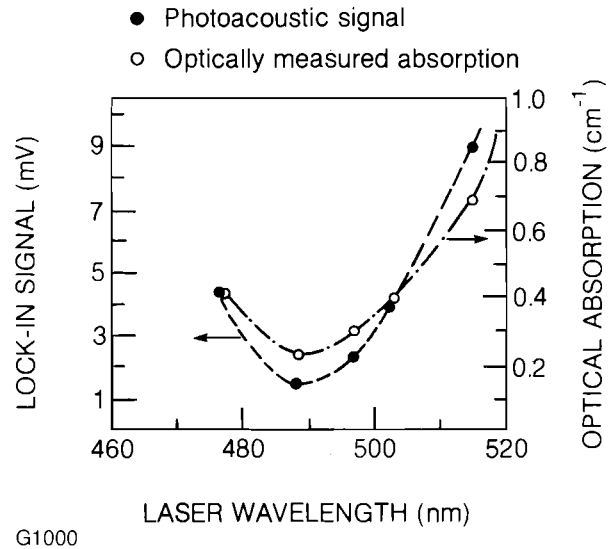
We have begun to utilize the photoacoustic absorption apparatus for the analysis of defects in dielectric thin film coatings composed of multiple alternating layers of high refractive index and low refractive index metal oxides. Such coatings are commonly employed to impart antireflecting, partly reflecting, or highly reflecting properties to the surfaces of lenses, windows, beamsplitters, and mirrors used in LLE's OMEGA laser system. Spatter is a type of defect sometimes found in these coatings, which occurs when materials being evaporated onto a substrate are instead ejected from the source as small, unevaporated particles. Oxidation of evaporants during coating deposition and post-deposition baking is required to impart appropriate mechanical and optical properties to a multilayer coating. Spatter sites represent portions of a coating that are prevented from achieving proper stoichiometry and structure because they are significantly less reactive than evaporated material in an oxygen atmosphere. Because of their altered composition, spatter sites can exhibit optical absorption which is larger than that of the surrounding stoichiometric coating material.[7]

Nomarski microscopy was used to locate titanium dioxide spatter sites that were intentionally generated in a $TiO_2/SiO_2$ multilayer coating on a BK-7 substrate by the Optical Coating Facility of the Institute of Optics. Scanning photoacoustic absorption spectroscopy was subsequently performed over a 50 micron by 40 micron region of the coating that contained one $TiO_2$ site 10 microns in diameter. PAS scans taken at

five laser wavelengths are shown in Fig. 7. The anomalously large absorption of this spatter site compared to the coated background is apparent. An inspection of the figure also shows that the absorption at this site increases as the laser wavelength decreases from the green to the
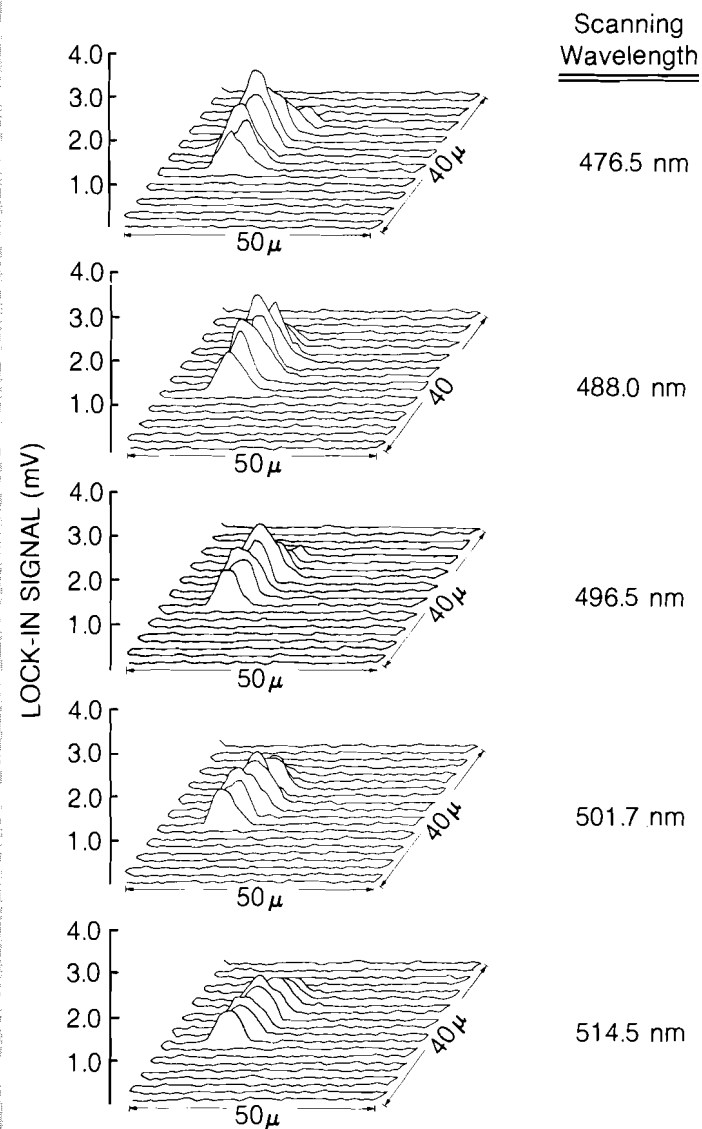


Fig. 7
Scanning photoacoustic absorption spectroscopy of a $TiO_2$ spatter site embedded in a $TiO_2/SiO_2$ multilayer dielectric thin film coating. The laser intensity at each wavelength was kept constant at a level of 145mW.

blue. By plotting the peak photoacoustic signal detected in each scan versus wavelength, the dispersion curve in Fig. 8 is obtained. From this curve it is evident that the wing of the ultraviolet absorption edge for the material in this spatter site begins at a wavelength near 500 nm. Optical spectrophotometry on a single 700 Å thick stoichiometric layer of $TiO_2$ indicates, however, that this wing should not be apparent until a wavelength of 350 to 400 nm. It is clear from this example that PAS offers an

Fig. 8
*Wavelength dispersion of the absorption in the $TiO_2$ spatter site as measured by plotting the maximum photoacoustic signal from each wavelength scan in Fig. 7. The increase in absorption observed to begin here at a wavelength of 500 nm commences in $TiO_2$ of proper stoichiometry at a lower wavelength near 350 nm to 400 nm.*
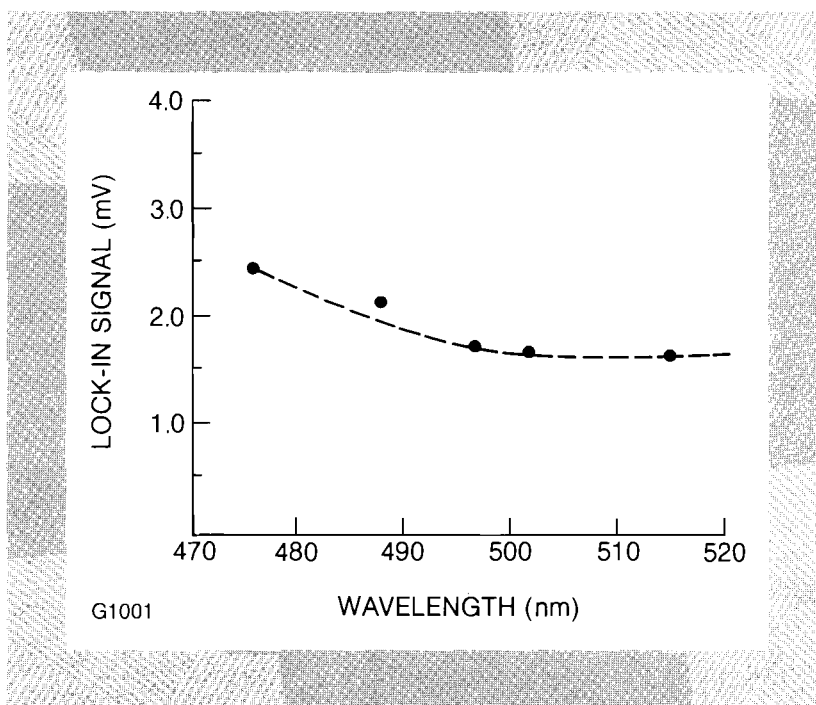
excellent means for non-destructively probing small defects in dielectric thin films to elicit their absorptive behavior.

Photoacoustic absorption spectroscopy in conjunction with other optical microanalytical techniques should, in future work, contribute to our understanding of defects in multilayer dielectric thin films. The characterization of defect properties such as optical absorption can lead to their identification, and a modification in coating deposition procedures to reduce defect number densities will ultimately increase the laser-damage resistance of coated laser system components.

REFERENCES
1. T. A. Wiggins, T. W. Walker and A.H. Guenther, *NBS Special Publication 620: Laser-Induced Damage in Optical Materials*, 277-286 (1980).

2. W. H. Lowdermilk and D. Milam, *IEEE J. Quantum Electron.* QE17, 1888 (1981).

3. R. P. Freese and K. Teegarden, *NBS Special Publication 568: Laser-Induced Damage in Optical Materials*, 313-332 (1979).

4. R. D. Jacobs, MS Thesis, Institute of Optics, University of Rochester (1979).

5. D. S. Atlas, MS Thesis, Institute of Optics, University of Rochester (1981).

6. J. Ravey and S. Premilat, *J. Chim. Phys.* 6-7, 1913-1921 (1970).

7. W. Heitman, *Appl. Opt.* 10 (11) (November 1971).

# Section 2
# PROGRESS IN LASER FUSION

## 2.A Initial Long-Pulse Experiments on OMEGA

During the months of August and September the first multi-beam experiments were performed on OMEGA with laser pulses approaching 1 nsec in duration. Our goal was to conduct a preliminary examination of some of the requirements necessary for the uniform ablative drive of spherical targets for direct-drive laser fusion.

A considerable effort was made to first characterize the performance of the OMEGA laser in the long pulse width regime. Measurements were performed to determine the passive and active transmission factors for all driver line and beamline optical components. Near and far-field energy distributions and beam phase front distributions taken with a grating interferometer[1] were used to gain confidence in the predictive capabilities of the two-dimensional beam propagation code MALAPROP. In addition, with the knowledge of the output intensity distribution and the relative phase front distribution, it was also possible to predict, with the aid of the code BEAMPROP, the expected intensity distribution in the target plane, and to compare this with the measured equivalent target plane distribution recorded in the BDP (beam diagnostic package) structures. Figure 9a shows a radially-averaged plot of the measured output near-field intensity profile which, when coupled with the measured radial extent of spherical aberration (Fig. 9b) gives, through the code BEAMPROP, a predicted intensity distribution in the target plane of the form shown in Fig. 9c. This can be compared with the actual measured distribution, a two-dimensional intensity plot of which is shown in Fig. 9d. Apart from the periodicity in the annular ring struc-
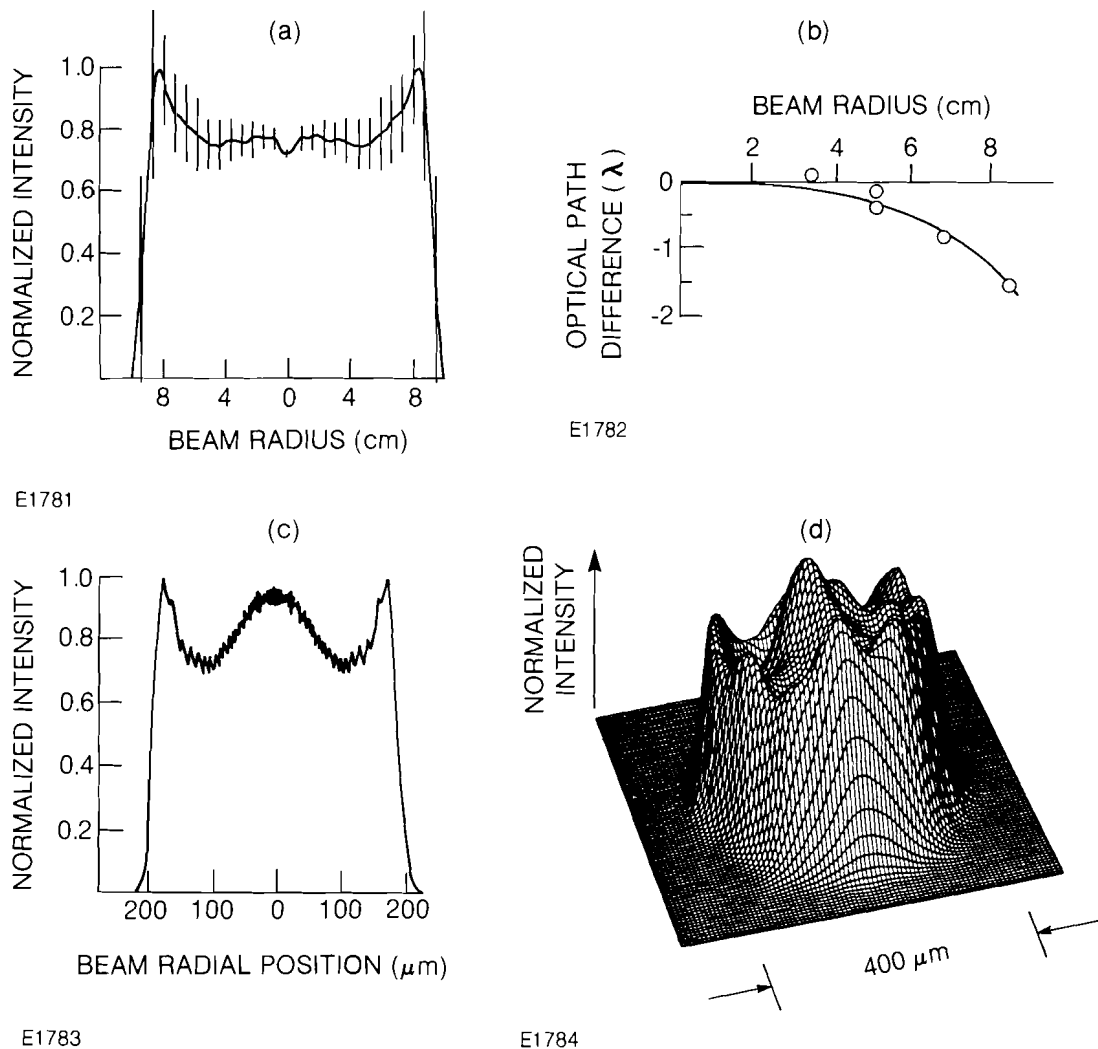
E1781

E1782

E1783

E1784

*Fig. 9*
*Comparison of actual and computed beam distributions in the target plane. From the actual radially-averaged near-field intensity profile (a) and the measured spherical aberration across the output beam (b), the code BEAMPROP predicts an intensity distribution in the target plane 1200 μm from best focus, of the form shown in (c), for a 17 cm beam focussed by a 600 mm lens. This can be compared with the equivalent target plane distribution measured in the BDP, shown in (d).*

ture seen in the equivalent target plane data of Fig. 9d (possibly caused by phase distortions resulting from the twelve-flash-lamp arrangement in the final amplifiers), there is good agreement between this measurement and the code prediction.

Target experiments with twelve well-characterized beams of OMEGA were conducted at 700 psec in a spherical irradiation geometry to compare the predictions of the one-dimensional hydrodynamic code, *LILAC*, and the two-dimensional Eulerian code, *SAGE*, with measurements of absorption in the intensity range between $10^{14}$ and $10^{15}$ W/cm². Laser absorption depends on target Z at $10^{14}$ W/cm², where the dominant mechanism is inverse bremsstrahlung. As the intensity is increased to the $10^{15}$ W/cm² level, the collisionless process of resonance absorption becomes important. This latter process results in the copious generation of super-thermal electrons, which redistribute energy to regions of

the target remote from the interaction zone, couple a significant fraction of their energy into fast ion expansion, and perhaps more seriously, preheat the core fuel to undesirably high temperatures.

Measurements of the variation in overall absorption for high Z (Ti) and low Z (CH) spheres 400 $\mu$m in diameter were performed with an array of 20 plasma calorimeters symmetrically distributed within the OMEGA target chamber. The results are shown in Fig. 10. From Fig. 10a it can be seen that peak absorptions of 70% are measured for Ti spheres at intensities around $10^{14}$W/cm². This absorption fraction drops to 50% as the intensity is increased. Similar behavior is observed for CH spheres (see Fig. 10b), except that the low intensity absorption is predictably lower in

*Fig. 10*
*Variation of absorption with intensity for 700 psec pulses incident uniformly on 400 $\mu$m diameter spheres of (a) Ti and (b) CH. The solid line represents comparative calculations made with the code SAGE, assuming inverse bremsstrahlung absorption, flux inhibition (f = 0.03) and a 15% deposition of energy reaching the critical surface into fast electrons.*



E1472

E1473

CH versus Ti, because it is a low Z target material. The solid lines in Fig. 10 represent *SAGE* calculations, taking into account both inverse bremsstrahlung and resonance absorption. The *SAGE* code correctly models the lack of a strong Z dependence to absorption at intensities approaching $10^{15}W/cm^2$. Predictions from the one-dimensional hydrodynamic code *LILAC* show a similar dependence.

The transition between absorption mechanisms was further investigated by measuring the spectrum of high energy ions using two Thompson parabola ion spectrometers equipped with CR-39 track detectors. This diagnostic permits the determination of absolute fluence and the energy spectrum for specific ionic species emitted from CH targets. The absorbed energy that was coupled into these ions (protons and ionized carbon $C^{6+}$, $C^{5+}$, $C^{4+}$, and $C^{3+}$) was determined as a function of laser intensity and compared to predictions from the *LILAC* code. The variation of the normalized energy partition to ions having energies in excess of 100 keV, as a function of intensity is shown in Fig. 11. The shaded area represents one-dimensional *LILAC* simulations of these experiments under the assumption of thermal flux-inhibition (f = 0.05) and 10%-15% deposition of energy at the critical density into super-thermal electron emission.



E1948
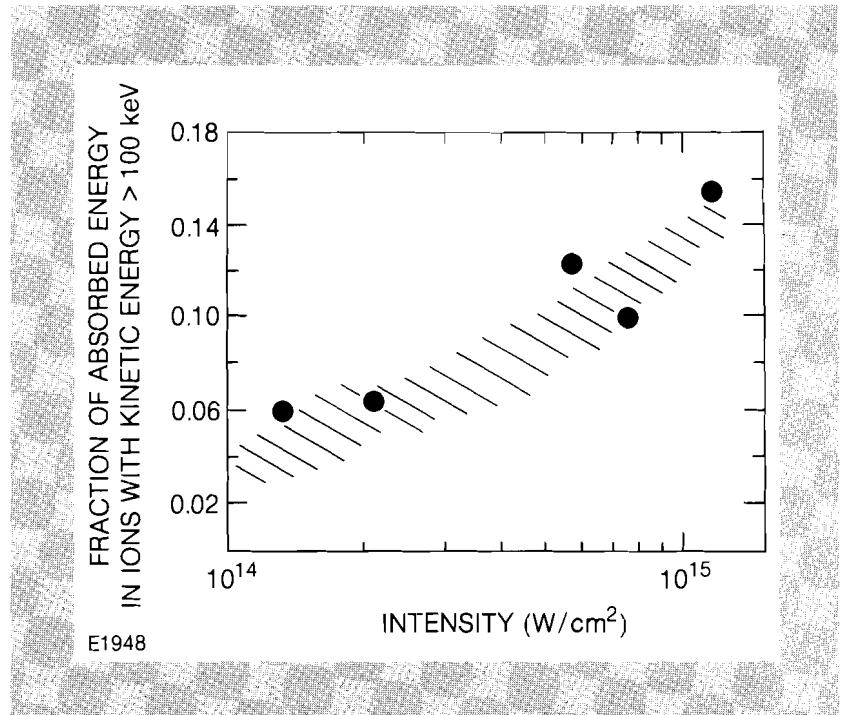
*Fig. 11*
*Variation of the partition of energy into ions having an energy in excess of 100 keV, as a function of intensity.*

The experiments described above have given us a preliminary look at the physics of symmetric implosions produced by long laser pulses. Much additional work in this area is planned for the coming months, and a concentrated effort will be directed toward measuring and understanding the limitations of thermal electron transport in this ablative regime.

REFERENCES
1. S. Kumpan, Preliminary LLE Report, June 1981.

# 2.B Filamentation of Laser Light in Flowing Plasmas

The filamentation of laser light entering a laser-plasma corona has been of much recent interest,[1,2,3] as it may significantly affect the absorption efficiency and implosion uniformity of laser fusion experiments. Previous calculations[4] of this instability have employed a static pressure-balance equation to represent the plasma response to the ponderomotive force. Generally, however, the plasma will be moving with respect to the filaments, and so it is more realistic to use hydrodynamic equations to determine the plasma response. Here we examine the effects of plasma flow on the thresholds and growth rates for filamentation.

The geometry of the instability is shown in Fig. 12. Filamentation may be "seeded" by hot spots in the incident beam or refraction by density fluctuations in the outer corona. These initial intensity variations are
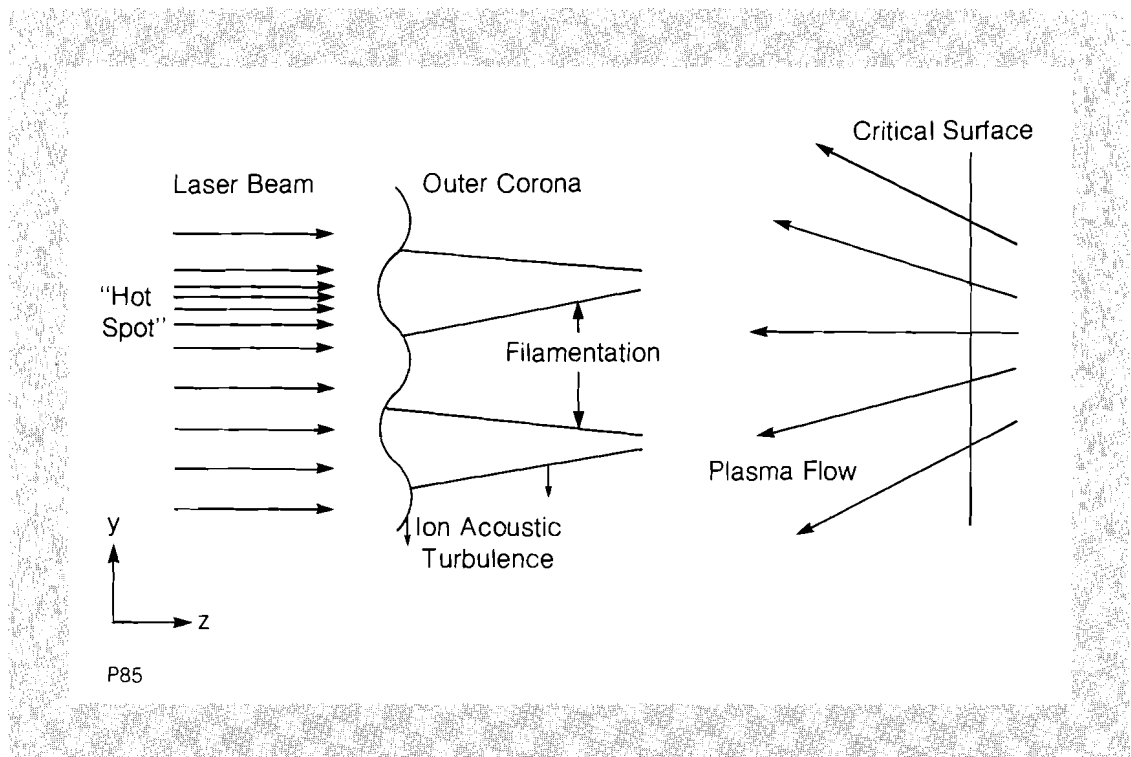


Fig. 12
Filamentation instabilities in laser-produced plasmas. Filamentation may be "seeded" by hot spots in the laser beam or refraction by density fluctuations in the outer corona.

then amplified by the instability. To calculate the spatial growth rate we work in the frame in which the critical surface and the intensity variations are stationary, and look for time-independent modes amplifying in the z-direction. For filaments arising from hot spots this will be the lab frame; for filaments arising from ion acoustic noise it will be a frame moving transverse to the incident light at approximately $c_s$, the ion sound speed. In this coordinate system we expect plasma flow velocities on the order of $c_s$ in the z-direction, and somewhat less than this in the y-direction. (Of course, we could use the frame in which the flow velocity vanishes, but this would entail the solution of time-dependent equations and matching the solution to the moving perturbations.)

To obtain the growth rate for the instability, we consider the simple case in which the plasma and incident beam are uniform except for small perturbations in density and laser intensity. Solving the resulting linear electromagnetic and fluid equations, we obtain the dispersion relation for filamentation in flowing plasma:

$$\left[ \frac{(n_0/2\varepsilon_0 n_c)\,(v^2_{osc}/v^2_{th})\,(1+q^2)}{1+q^2+(i\nu/k_y c^2_S)\,(v_{oy}+qv_{oz})-(v_{oy}+qv_{oz})^2/c^2_S} - x^2\,(1+q^2) \right] x^2\,(1+q^2)$$

$$+ 4x^2 q^2 = 0 \qquad (1)$$

Here $n_0$ is the equilibrium density, $v_{oy}$ and $v_{oz}$ are the $y$ and $z$ components of the fluid velocity, respectively, $n_c$ is the critical density for the laser light, $v_{osc}$ is the quiver velocity of an electron in the electric field of the light, $v_{th}$ is the average electron thermal velocity, $\nu$ is the damping rate of ion-acoustic waves, $k_y$ and $k_z$ are the $y$ and $z$ components of the wavevector of the perturbation, $k_0$ is the wavenumber of the incident light, $x = k_y/k_0$, $q = k_z/k_y$, and $\varepsilon_0 = 1-n_0/n_c$. The spatial growth rate for the instability is given by the imaginary part of $q$. Equation (1) is our main result; in the following, we examine some of its consequences.

First we consider the effect of the transverse velocity $v_{oy}$, taking $\nu = v_{oz} = 0$. Assuming $|q| \ll 1$ the threshold condition becomes:

$$q^2 = \frac{x^2}{4} - \left(1 - \frac{v^2_{oy}}{c^2_S}\right)^{-1} \frac{n_0}{8\varepsilon_0 n_c} \frac{v^2_{osc}}{v^2_{th}} < 0 \qquad (2)$$

This result agrees with Ref. (4) for $v_{oy} = 0$ and indicates that thresholds decrease and growth rates increase as $|v_{oy}|$ increases for $|v_{oy}| < c_S$; for $|v_{oy}| > c_S$ no growth occurs. The discontinuity in growth rate for $|v_{oy}| = c_S$ is due to breakdown of the assumption $|q| \ll 1$; to elucidate the actual behavior of the instability for $v_{oy} \sim c_S$ we plot solutions of the full dispersion relation (1) in Figs. 13(a) through 13(e). The solutions of (1) which represent filamentation are those roots which are continuous with the roots of (2) as a function of $v_0$; other complex roots of (1) may be shown by Briggs-Bers analysis[5] to be evanescent, except for a small range of $v_0$ where they represent Brillouin scattering. Figs. 13(a) through 13(c) show the effects of transverse velocity at various incident intensities for a typical value of $k_y$ and no damping. In Figs. 13(a) and 13(b) filamentation is below threshold for $v_{oy} = 0$ but grows for a range of $v_{oy}$ around $v_{oy} \sim c_S$. The range of instability increases with increasing $v_{osc}/v_{th}$ until in Fig. 13(c) growth occurs even when $v_{oy} = 0$, though the growth rate still increases significantly as $v_{oy} \rightarrow c_S$. These plots also show that for $v_{oy} \sim c_S$ $k_z$ has a real as well as an imaginary part, indicating that the filaments will grow at an angle to the incident light (they are perpendicular to Re($\underline{k}$)). Figures 13(d) and 13(e) show the effect of including Landau damping of ion motion. The maximum spatial growth rates are reduced but the instability grows for a wider range of transverse velocities. Finally, calculations with varying $v_{oz}$ show that the component of flow velocity parallel to the incident light has little effect on filamentation.
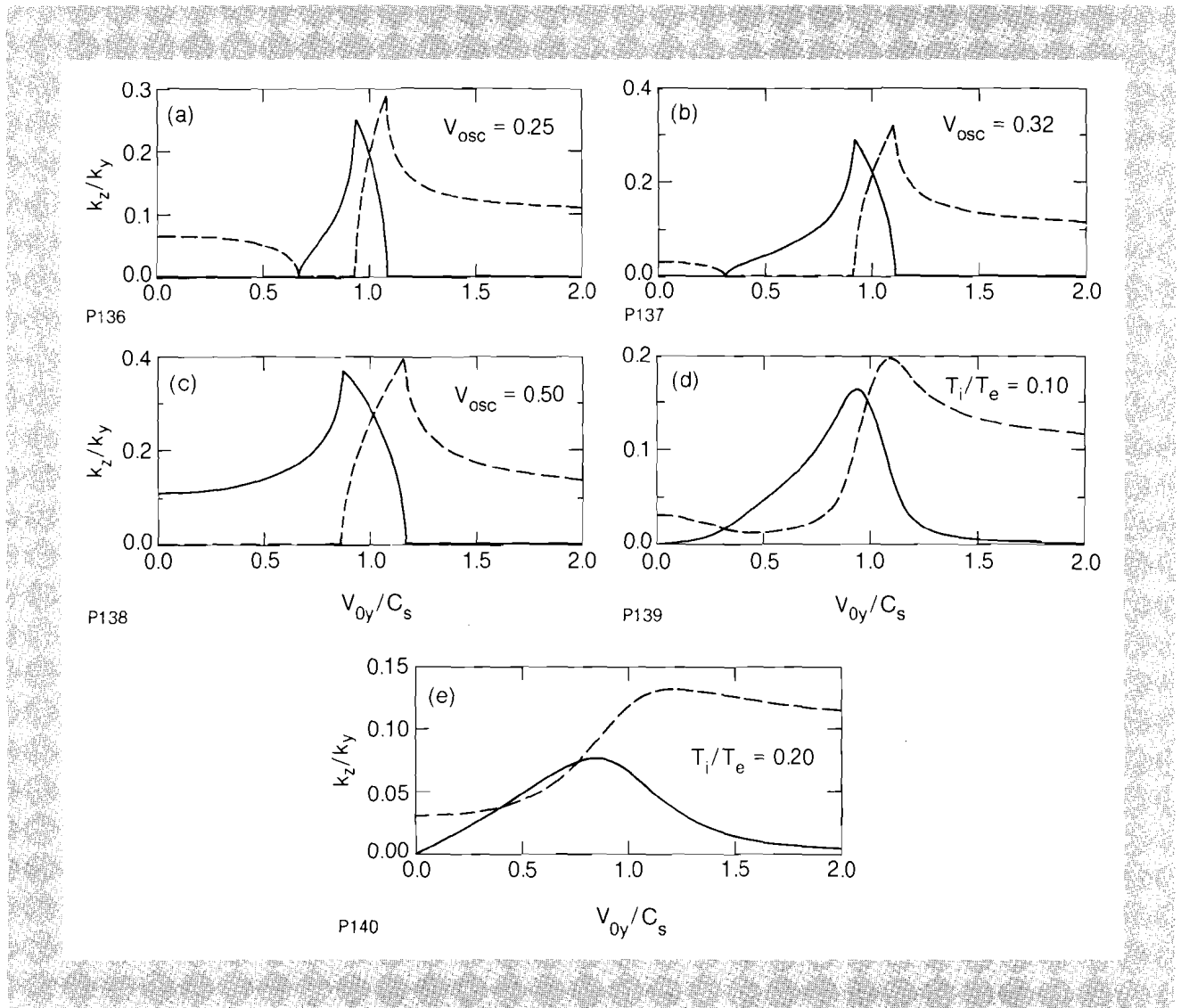
*Fig. 13*
*Real (dashed) and imaginary (solid) parts of solutions to filamentation dispersion relation. For (a)-(c), $k_y/k_0 = 0.2$, $v_{oz} = 0$, $T_i/T_e = 0$. For (d)-(e), $k_y/k_0 = 0.2$, $v_{oz} = 0$, $v_{osc}/v_{th} = 0.32$.*

In conclusion, we have derived the dispersion relation for filamentation in flowing plasmas. We find that flow velocities transverse to the incident light decrease thresholds and increase spatial growth rates. This result may be especially significant for filamentation due to refraction from acoustic turbulence in the outer corona, which may be expected to have significant transverse velocities.

REFERENCES

1. O. Willi and P. T. Rumsby, *Opt. Comm.* **37**, 45 (1981).

2. M. J. Herbst, J. A. Stamper, R. R. Whitlock, R. H. Lehmberg, and B. H. Ripin, *Phys. Rev. Lett.* **46**, 328 (1981).

3. R. Bingham, R. Short, E. Williams, D. Villeneuve, and M. Richardson, to be published in *Proc. of Topical Conference on Symmetry Aspects of Inertial Fusion Implosions*, NRL, May 1981.

4. P. Kaw, G. Schmidt, and T. Wilcox, *Phys. Fluids* **16**, 1522 (1973).

5. R. J. Briggs, *Electron-Stream Interactions with Plasmas* (MIT Press, Cambridge, Mass., 1964).

# Section 3
# DEVELOPMENTS IN
# MICROFABRICATION

## 3.A Improvements in Nonconcentricity
## Measurement of Target Shells

An improved technique has been developed for characterizing the thickness uniformity of target shells used as fuel containers in laser fusion experiments. A requirement for these target shells is that they have walls uniform in thickness to preserve implosion symmetry.[1] The usual interferometric technique[2,3] for characterizing shell uniformity has been modified to improve the detection sensitivity to shell concentricity defects. This modification, which simply involves adding gas to the shell, can provide up to five times the sensitivity to this type of defect. No additional equipment is required to achieve the improvement. Interpretation of the shell interferograms is made by knowing the shell material, diameter and average wall thickness, and the gas index of refraction.

Figure 14 is a cross section of a nonconcentric shell of diameter D and average wall thickness $t_O$. A transmission interferometer visually displays the optical path difference (O.P.D.) between light rays passing through the shell (ray 1) and rays passing by the shell (ray 2). The O.P.D. is displayed as contours spaced at one-wavelength intervals. These contours, or interference fringes, are concentric with the geometric center of the shell if the nonconcentricity ratio $\Delta t/t_O = 0.0$. If $\Delta t/t_O > 0.0$, the O.P.D. contours are not concentric with, but displaced from, the geometric center of the target by a distance S. The quantity S/D is the interferogram asymmetry ratio which is measured by the interferometer operator.

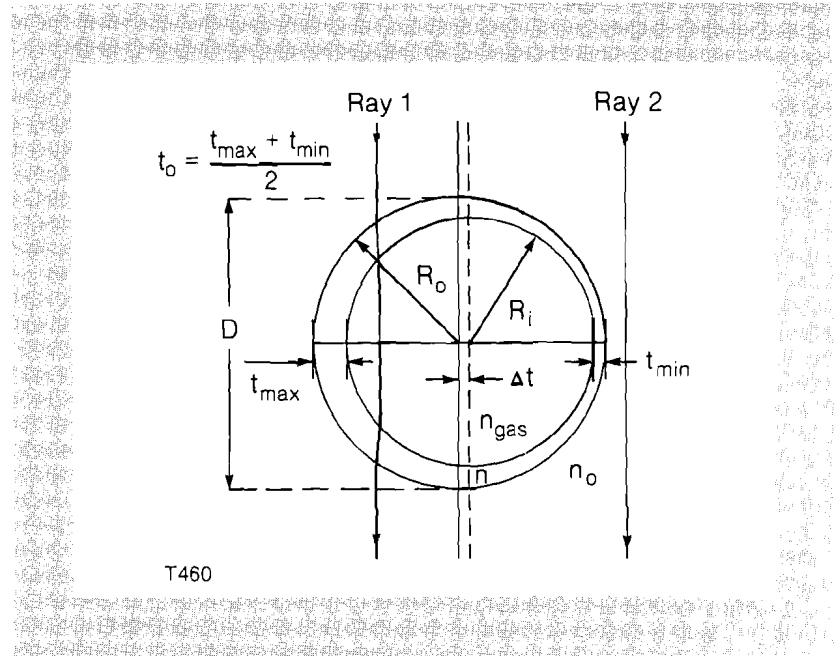A first order, non-refracting analytical analysis of this problem gives

Fig. 14
Diagram of a nonconcentric transparent shell illustrating important features. Examples of collimated light passing through and around the shell are given by rays 1 and 2.

the following relationship between the nonconcentricity ratio $\Delta t/t_0$ and the interferogram asymmetry ratio $S/D$.

$$\frac{\Delta t}{t_0} = \frac{Q(1 + \dfrac{2t_0}{D}) - 1}{Q\dfrac{t_0}{D}} \cdot \frac{S}{D} \tag{3}$$

where

$$Q = 1 - \left[\frac{P(n_{gas} - 1)}{n - 1}\right] \tag{4}$$

Here P is the shell gas fill pressure in atmospheres, $n_{gas}$ is the gas refractive index for 1 atmosphere pressure and n is the refractive index of the target shell.

These analytical results were compared with an exact computer ray trace computation. Rays were traced through target shells having various nonconcentricity ratios and gas fills. The results of the analytical model and the exact ray trace solution are shown in Fig. 15. They exhibit similar behavior. The simplicity of the first order analytical model makes it suitable for indicating trends only. Because physical processes such as refraction are ignored, this model is limited to predicting that increased gas pressure within a target shell increases the observed asymmetry ratio $S/D$ for a fixed value of $\Delta t/t_0$. The ray trace verification of this prediction demonstrates that enhanced interferometric sensitivity to small values of $\Delta t/t_0$ result for high pressure gas fills in shells.

The universal (dimensionless) series of curves in Fig. 15 for the more accurate ray trace treatment may be used to derive target shell nonconcentricity information from interferometrically measured fringe asymmetry for a reasonably broad range of gas fill pressures. The gas pres-

Fig. 14
*Diagram of a nonconcentric transparent shell illustrating important features. Examples of collimated light passing through and around the shell are given by rays 1 and 2.*

the following relationship between the nonconcentricity ratio $\Delta t/t_0$ and the interferogram asymmetry ratio $S/D$.

$$\frac{\Delta t}{t_0} = \frac{Q(1 + \frac{2t_0}{D}) - 1}{Q \frac{t_0}{D}} \cdot \frac{S}{D} \tag{3}$$

where

$$Q = 1 - \left[\frac{P(n_{gas} - 1)}{n - 1}\right] \tag{4}$$

Here P is the shell gas fill pressure in atmospheres, $n_{gas}$ is the gas refractive index for 1 atmosphere pressure and n is the refractive index of the target shell.

These analytical results were compared with an exact computer ray trace computation. Rays were traced through target shells having various nonconcentricity ratios and gas fills. The results of the analytical model and the exact ray trace solution are shown in Fig. 15. They exhibit similar behavior. The simplicity of the first order analytical model makes it suitable for indicating trends only. Because physical processes such as refraction are ignored, this model is limited to predicting that increased gas pressure within a target shell increases the observed asymmetry ratio S/D for a fixed value of $\Delta t/t_0$. The ray trace verification of this prediction demonstrates that enhanced interferometric sensitivity to small values of $\Delta t/t_0$ result for high pressure gas fills in shells.

The universal (dimensionless) series of curves in Fig. 15 for the more accurate ray trace treatment may be used to derive target shell nonconcentricity information from interferometrically measured fringe asymmetry for a reasonably broad range of gas fill pressures. The gas pres-
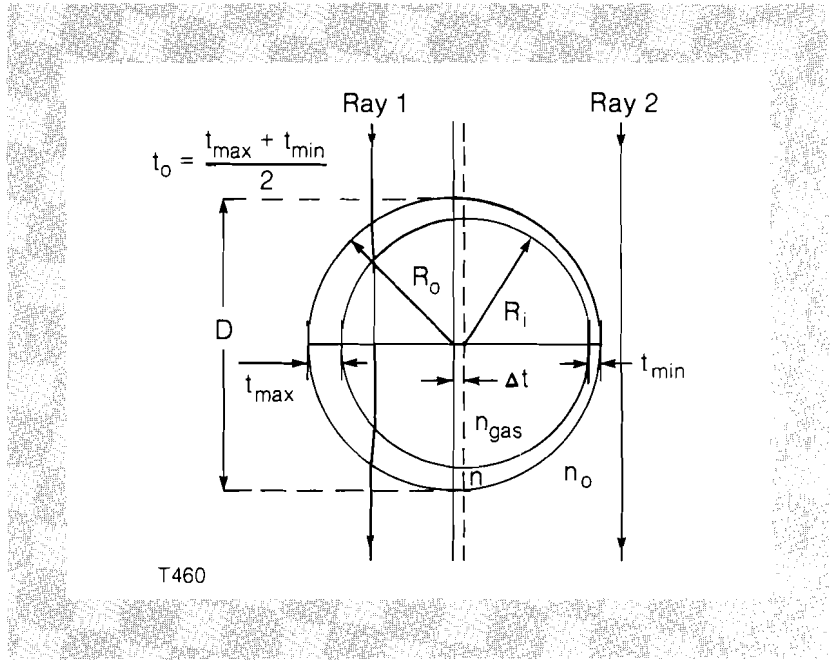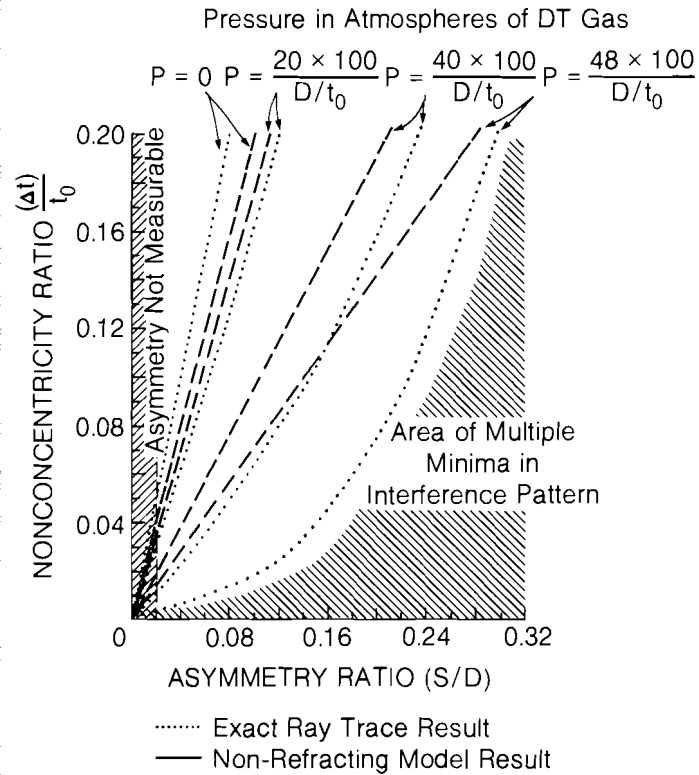
sures plotted in Fig. 15 are normalized by the ratio of target shell diameter to shell thickness $D/t_0$. Complications in interpreting the measurement of target shell concentricity result at very high gas fill pressures. The cross-hatched area on the right side of Fig. 15 indicates this region where care must be exercised.



Pressure in Atmospheres of DT Gas

$$P = 0 \quad P = \frac{20 \times 100}{D/t_0} \quad P = \frac{40 \times 100}{D/t_0} \quad P = \frac{48 \times 100}{D/t_0}$$

NONCONCENTRICITY RATIO $\frac{(\Delta t)}{t_0}$

Asymmetry Not Measurable

Area of Multiple Minima in Interference Pattern

ASYMMETRY RATIO (S/D)

········· Exact Ray Trace Result
——— Non-Refracting Model Result

T461

*Fig. 15*
*Universal curves relating nonconcentricity and fringe asymmetry are plotted for glass shells. Both the analytic model and ray-trace results are shown.*

A capillary mounted target shell[4] has been used to experimentally verify our improved nonconcentricity characterization procedure. A measured pressure of gas is introduced into the shell through the hollow stalk. Figure 16a shows an interferogram of a glass shell mounted on the capillary stalk and filled with one atmosphere of air.

The asymmetry ratio measured from Fig. 16a is $S/D = 0.08$ which, from Fig. 15, corresponds to a nonconcentricity ratio of $\Delta t/t_0 = 0.20$. An interferogram of this same glass shell at a fill pressure equivalent to 34 atmospheres of a DT mixture is shown in Fig. 16c. The measured asymmetry, now much larger, is equal to $S/D = 0.30$. The measurable quantity, shell asymmetry, has been increased in size by a factor of 3.75 simply by adding 34 atmospheres of gas to the shell. This increased detection sensitivity to small nonconcentricity defects is the improvement obtained from the modified approach. Small defects previously not visible in the interferograms can now be measured. Computer-generated contour plots from shells having the same dimensions and fill pressures as

shown in Figs. 16a and 16c are reproduced in Figs. 16b and 16d respectively. The computer-generated plots show shell contours at 0.1 fringe increments, but are otherwise similar to the experimentally measured interferograms.
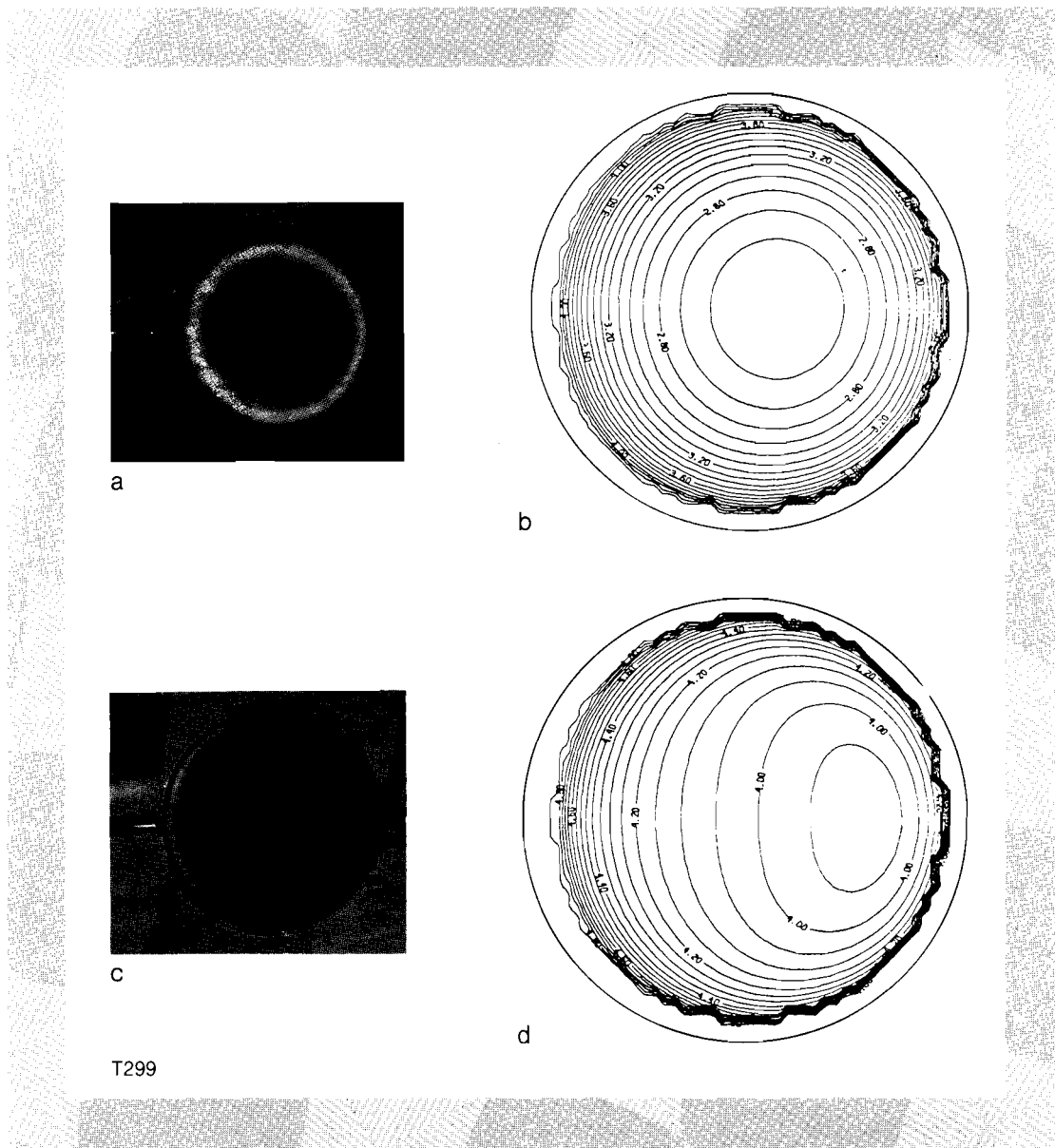


T299

Fig. 16
*Comparison of experimental and analytical examples of shell nonconcentricity: (a) Interferogram of shell with 1 atmosphere air pressure. (b) Computer-generated contour plot of O.P.D. for a shell with 1 atmosphere pressure. (c) Interferogram of the same shell as in (a) but with a gas refractive index equivalent to 34 atmospheres of DT. (d) Computer-generated contour plot of O.P.D. as in (b) but with 34 atmospheres of DT.*

The above comparison between measured and modeled results for the gas-filled shells shows excellent agreement. Predictions made from the simple analytical analysis, that improved detection sensitivity is derived by adding gas to target shells, have been verified. A non-dimensional series of curves, which shows the increased detectability to shell nonconcentricity gained by adding gas to the shell, has been given.

REFERENCES
1. G. Fraley, W. Gula, D. Henderson, R. McCrory, R. Malone, R. Mason and R. Morse, *Plasma Physics and Controlled Nuclear Fusion Research*, Paper IAEA-CN-33/F5-5, page 543 (1974).

2. R. R. Stone, D. W. Gregg and P. C. Souers, *J. Appl. Phys.* **46**, 2693 (1975).

3. B. W. Weinstein and C. D. Hendricks, *Appl. Opt.* **17**, 3641 (1978).

4. B. Brinker, J. R. Miller, "Capillary Gas Filling of Inertial Fusion Targets," *J. Vac. Sci. Technol.* (to be published).

## 3.B Progress in Ablation Layer Fabrication

An ablatively driven inertial fusion experiment requires a precise, layered target consisting of concentric spherical shells. Incident laser radiation is absorbed at the critical density surface of the outermost layer called the ablation layer. Thermal conduction then carries the absorbed energy inward from the critical density surface and heats adjacent layers of material which expand radially outward. To conserve the momentum associated with this expansion, the material comprising the inner layers of the target implodes. To achieve uniform implosions and prevent hydrodynamic instability, the ablation layer must be uniform in thickness and density, and its surface irregularity must be minimized.

The ablation layer consists of low Z materials, most commonly polymeric hydrocarbons. Layers of this type have been deposited on shells in a variety of ways. One method employed at LLE involves the vapor phase pyrolysis of di-para-xylylene. In this process the di-para-xylylene molecule is sublimated and, upon heating to 600° C in vacuum, pyrolyzes into two monomers. The monomers deposit onto a room temperature substrate, instantly polymerizing into poly-para-xylylene, or parylene.

This deposition process is unique in that it produces an ablation layer free of pinholes that conforms well to the target surface. The rate of layer deposition is relatively fast. The disadvantages of this technique are 1) the method is material specific and works only for di-para-xylylene and its derivatives, and 2) the resultant crystalline texture of parylene introduces small-scale density fluctuations in the coating and also promotes a coarse surface finish. A coating density variation of 5 percent and a surface roughness of 1 $\mu$m work against uniform implosions of laser fusion targets, but they are characteristic of the inherent crystalline texture of pure parylene films, which are approximately 60 percent by volume crystalline.

Transforming this polymer material to an amorphous structure will cause the resulting film to be smoother, and the density fluctuations to be dramatically diminished. Because crystallization occurs simultaneously with polymerization, retardation of crystallization can be accomplished by increasing the complexity and bulky nature of the intermediate monomer stage. In fact, it has been shown that chlorine substituted monomers result in more amorphous parylene films than those obtained from unmodified di-para-xylylene.[1] At LLE, we have been modifying the structure of the di-para-xylylene starting material so that less

crystalline parylene films may be obtained.

In order to limit the composition of the ablation layer to hydrocarbons, the modification of di-para-xylylene was done with alkyl groups only. As reported earlier,[2] alkyl substituted di-para-xylylenes were produced via a Freidel-Crafts electrophilic substitution using aluminum chloride as the Lewis acid.[3] (2,2) paracyclophane (di-para-xylylene) was reacted with alkyl halide in the presence of aluminum chloride and the catalyst was neutralized by hydrolysis. The resulting alkylated (2,2) para-cyclophane was purified by recrystallization. With the above procedure we have prepared ethyl, isopropyl, and normal butyl (2,2) para-cyclophanes whose structures have been verified by infrared and NMR spectroscopy. Since no improvement in coating surface finish is accomplished from the use of longer alkyl pendant groups and because the yield and purity of the product decreases with longer chain length, we have selected ethyl di-para-xylylene as the starting dimer of choice for our work.

Alkylation of di-para-xylylene introduces significant changes in the properties and structure of the resulting polymers. Crystallinity, melting temperature $(T_m)$, and glass transition temperature $(T_g)$ of the pure polymer decrease when modified. These changes are tabulated in Table 2. X-ray diffraction studies[4] indicate that alkyl modification does not alter the monoclinic unit cell structure. Unit cell dimensions of several alkyl-substituted and a chloro-substituted poly-para-xylylenes are compiled in Table 3. As this table shows, the monoclinic cell $\beta$ angle is unchanged.

Table 2
Physical properties changes to parylene when alkylated. The addition of ethyl or isopropyl groups causes the melting and glass transition temperatures of parylene to decline. The crystallinity of the modified polymer is also reduced.

| Polymer | $T_m$, °C | $T_g$, °C | Crystallinity % |
|---------|-----------|-----------|-----------------|
| PPX | 442 | 180 | 59 |
| Et-PPX | 148 | 115 | 32 |
| iP-PPX | 64 | – | – |

T458

Table 3
Unit cell dimensions of alkylated parylenes. Only the cell length along the b-axis is affected by alkyl modification. $\beta$ is the angle formed by the a- and c-axes in the monoclinic lattice.

| Polymer | a(Å) | b(Å) | c*(Å) | $\beta$(degrees) |
|---------|------|------|-------|------------------|
| | ═══ Monoclinic Lattice ═══ | | | |
| PPX | 5.9 | 10.6 | 6.6 | 135 |
| Et-PPX | 5.9 | 13.4 | 6.5 | 135 |
| iP-PPX | 5.9 | 14.0 | 6.5 | 135 |

*the c-axis lies along the chain direction

T459

*Fig. 17*

*Surface smoothing by alkyl modification of di-para-xylylene. The surface finish of polymer films obtained by the deposition of alkylated di-para-xylylene improves significantly due to reduced crystallinity of the polymer.*

    *a) surface topology of poly-paraxylylene*

    *b) surface topology of ethyl poly-para-xylylene*

The lengths of the a-axis and c-axis remain constant but the length of the b-axis increases with the size of the pendant group. Since the c-axis lies along the chain direction and is parallel to the layer surface, the alkylated monomer is believed to form a polymer with the alkyl pendant group aligned perpendicularly to the layer surface.

X-ray diffraction experiments show ethyl parylene to consist of finely dispersed crystallites. The diminished crystallinity achieved with our alkyl modification serves a dual purpose. The surface roughness arising from crystalline texture is greatly diminished. Figure 17 shows that the ablation layer surface smoothness is better than 1000 Å. In addition, density fluctuations within the layer are minimized.



(a)

|———————————|
5 µm

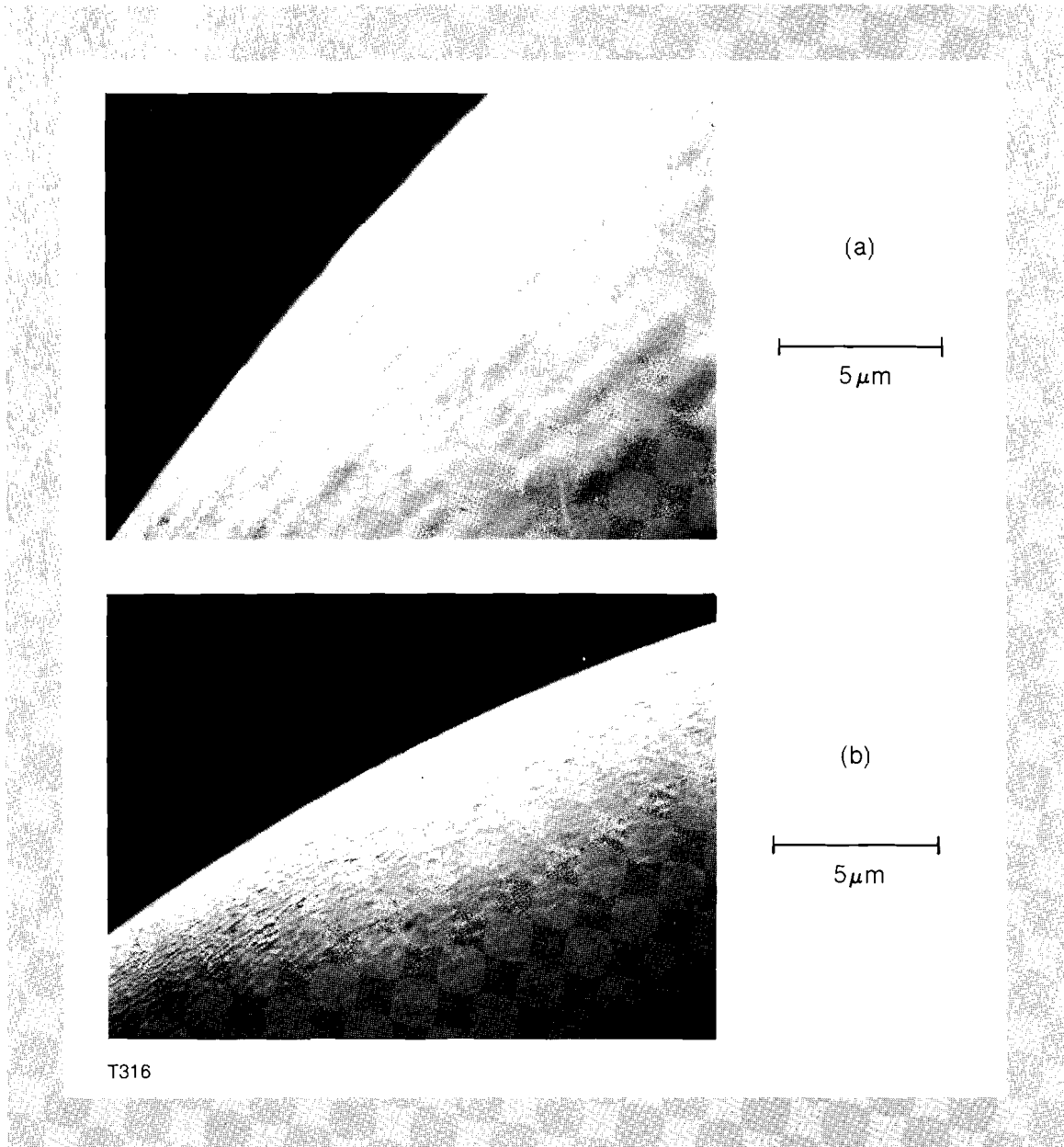T313



(b)

|———————————|
2 µm
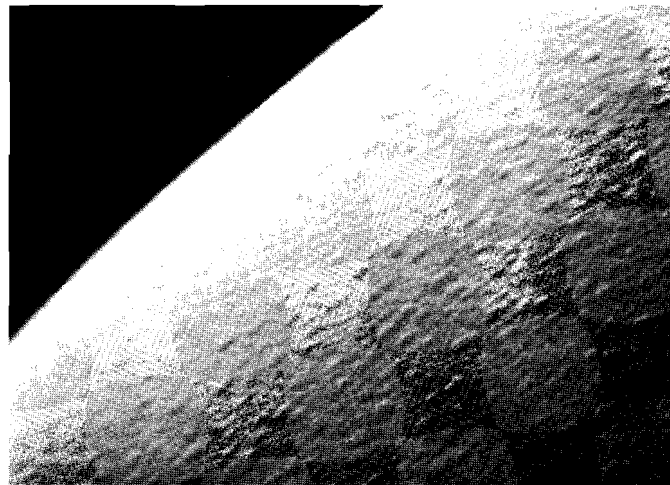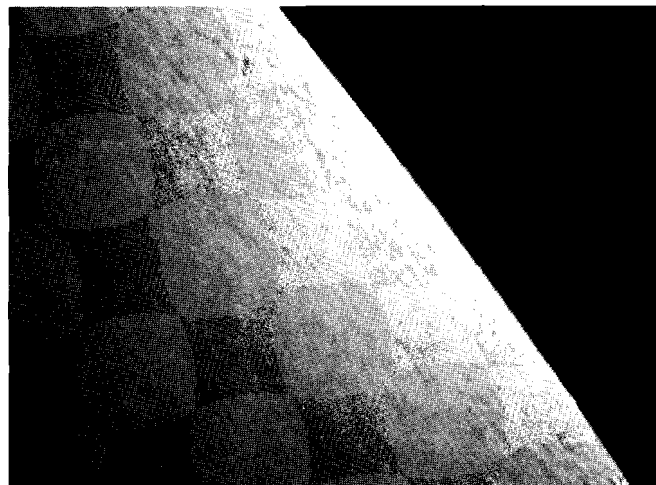
T314

An ancillary advantage to using ethyl di-para-xylylene arises from the ability to anneal ethyl parylene because of its reduced value of $T_g$. The 70 percent volume fraction of ethyl parylene, which exists in a glassy state, can be made to flow by heating the coated target above $T_g$. Dimensional stability of the coating is retained during the annealing process because of the cross-linking provided by the dispersed microcrystalline phase. Melting of the crystal phase does not occur provided that the annealing temperatures are kept below $T_m$.

Geometrical surface defects can be reduced with the proper thermal annealing cycle of ethyl substituted parylene. The efficacy of annealing for the removal of cone defects[5] is shown in Fig. 18. Cone defects are frequently observed in ablation layers and originate from minute defects

*Fig. 18*
*Annealing of ethyl parylene films. Surface tension smooths away cone defects when thermal annealing of ethyl parylene films is performed. The layer's residual microcrystallinity preserves dimensional stability during the anneal.*

- *a) as coated ethyl parylene film showing cone defects.*
- *b) surface after annealing at 120 degrees C for 20 hours.*



(a)

5 μm

(b)

5 μm

T316

on the target surface during coating. The cone defects in Fig. 18a have a lateral size of several microns. After annealing the polymer at 120 degrees C for 20 hours, these defects disappear as shown in Fig. 18b. Other defects not originally present in Fig. 18a can be seen to have formed in Fig. 18b. Of much smaller size, these new defects form during the annealing cycle and are expected to be minimized through optimization of annealing parameters.

In summary, modification of the dimer di-para-xylylene via alkylation has resulted in the deposition of ethyl parylene ablation layer coatings on fusion targets with improved surface finish (1000 Å) and more uniform bulk density. This accomplishment is a direct consequence of reducing the polymer crystallinity from 60 percent to 30 percent. The modified polymer allows us to reduce, by thermal annealing, cone defects present on our ablation layer surfaces.

REFERENCES
1. H. Kim, unpublished work.

2. *LLE Review* 1, 40 (1979).

3. W. F. Gorham, *J. Polymer Sci.*, A-1, 4, 3027 (1966).

4. H. Kim and N. S. Murthy, *Bull. Amer. Phys. Soc.* 27, 331 (1982).

5. S. A. Letts, D. W. Myers and L. A. Witt, *LLNL Report* UCRL-84475, 8-2b (1980).

# Section 4
# DEVELOPMENTS IN SUBPICOSECOND RESEARCH

## 4.A Picosecond Electron Diffraction

Laser-induced structural kinetics in the picosecond time domain are of current interest in the field of solid state surface physics and semiconductor annealing. In the past, time-dependent structural kinetics have gone unmonitored for lack of a suitable picosecond x-ray or electron probe in synchronism with the laser pulse. Recently, subnanosecond x-ray bursts produced by a laser plasma have been successfully used by R. Frankel and J. Forsyth[1] to generate low angle x-ray diffraction patterns of biological samples. On a slightly longer time scale using synchrotron radiation, nanosecond studies of the kinetics of annealing have been made by B. C. Larson[2] and co-workers. In this article, we report on a technique which makes possible laser-induced structural kinetic studies in the picosecond range using a burst of electrons from the front end of the streak camera.

With the exception of picosecond photoelectron switching recently demonstrated,[3] streak camera tubes have been used exclusively as a fast optical or x-ray diagnostic tool. However, some of the most beautiful features of the image converter tube used in the streak camera have been only partially exploited with this application. The image converter tube produces a temporal and spatial monoenergetic photoelectron replica of an optical pulse. This replica is ultimately limited by the temporal and spatial resolution of the particular streak tube employed. With a relatively low input signal to minimize space charge broadening, the temporal and spatial resolution can be subpicosecond[4] and of the order of 100 $\mu$m respectively. Other features worth noting about this photo-

electron replica are that it is synchronized to within a picosecond with the original optical pulse[5] and can be operated at a high repetition rate.[6] These properties make the front end of the streak camera tube particularly well suited for picosecond electron diffraction.

Unlike x-rays which are more appropriate for examining bulk properties of a material, 20 keV electrons penetrate only a few hundred angstroms or less and thus investigate effects on or near the surface of a specimen. As shown in Fig. 19, our experimental layout is comprised of a demountable Photochron II streak camera tube with the deflection plates removed. An aluminum photocathode is used to allow the tube to be opened to air for insertion of the specimen under study. The specimen is located in the drift region of the streak tube 1 cm from the anode and 29 cm from the phosphor screen located downstream. The electron energy is 20 keV and corresponds to a wavelength of 0.86 Å. The specimen thickness is chosen according to the mass thickness parameter $\mu_s = \mu \cdot d$ where $\mu$ is the density of the specimen and d is its thickness. The mass thickness parameter must be of the order of $3 mg/cm^2$[7] for a 20 keV electron to experience a single elastic collision.



Optical Photoelectron Pulse Replica F A
Specimen
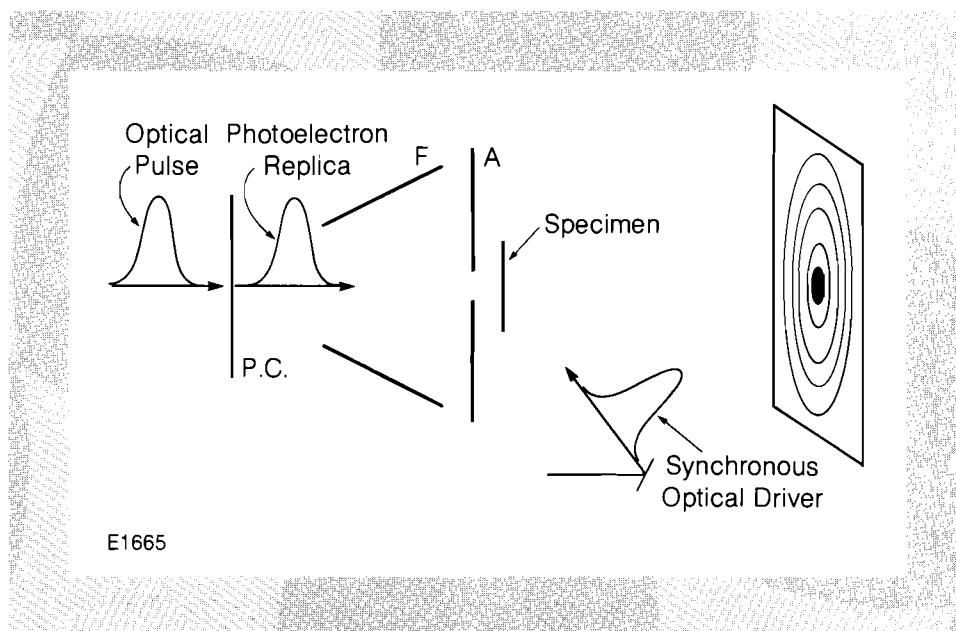P.C.
Synchronous Optical Driver

E1665

*Fig. 19*
*Experimental layout for generating a picosecond electron diffraction pattern. P.C. is the Al photocathode set at 20 kV, F is the focus cone, A is the anode set at ground potential. The system is evacuated to $10^{-6}mm$ Hg using an oil diffusion pump.*

The fourth harmonic from an active-passive mode-locked Nd:YAG laser is used to overcome the 4.1 eV work function of the aluminum photocathode. At this wavelength (266nm) the quantum efficiency for Al is approximately $10^{-5}$. The optical energy on the Al photocathode of the streak camera is approximately a few microjoules. The electron pulse width has been measured by using the camera on the normal streak mode, and is found to be 100 psec. This value departs significantly from the 15 psec pulse width expected. The pulse broadening is due to the space charge effect caused by the relatively high electron flux required to photograph the pattern with our present system. The spot size at the specimen is 3 mm, although a probing cross-section of a few hundred microns in diameter has been used with only a slight reduction in brightness. An image intensifier with a gain of about $10^4$ is used to amplify the pattern appearing on the screen.

Figure 20 shows the transmission electron diffraction pattern obtained with a single 100 psec electron pulse passing through a 150 Å thick aluminum specimen. Four distinct rings appear in this pattern. Their radii, after correction for the pincushion distortion of the image intensifier, are in the ratio 1:1.5:1.6:2, and indicate a face-centered cubic type crystal.[8] For each ring the lattice constant $a_O$ can be found using the Bragg relation for small angles,[8]

$$a_O = \frac{2\lambda\sqrt{k^2 + l^2 + m^2}}{r} \cdot L \tag{5}$$

where r is the ring radius, L is the distance between the specimen and the phosphor plane, k, l and m are the Miller indices, and $\lambda$ is the wavelength associated with the electron. For the four rings representing the diffracting planes 111, 200, 220, and 311 (listed radially outwards) we find the lattice constant $a_O = 4.03 \pm .08$ Å, in close agreement with the known lattice constant for aluminum of 4.05 Å.[8]
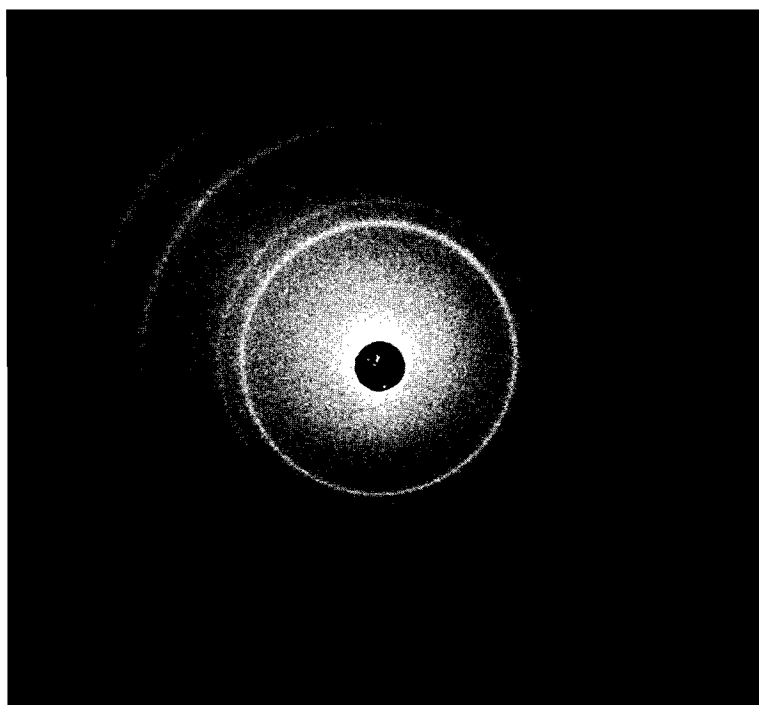


E1742

Fig. 20
Transmission electron diffraction pattern of aluminum from 100 psec exposure of 20 keV electrons. The specimen is 150 Å thick.

The simple experiment described above demonstrates how a short, synchronized electron burst generated by laser radiation impinging on the front end of a streak camera can be used to create an electron diffraction pattern from a thin specimen. Although this pattern is from an electron beam whose pulse width is 100 psec, we expect that this technique can generate electron pulse widths a few picoseconds in duration if presently used electron fluxes are reduced. It should be possible to decrease the electron flux level by a factor of over 100 by using a larger gain image intensifier directly contacting the recording film.

Part of our future work in time-resolved electron diffraction will be directed toward the deflection capabilities of streak camera tubes. By

operating the streak tube in saturation mode so that the space charge significantly broadens the pulse in time, it has been shown that the electron pulse generated in such operation broadens in time about the center, with a width dictated by the current density at the photocathode.[9,10] This temporal broadening can occur with a negligible increase in spot size. The elongated electron burst could be used to probe a specimen over the entire time span of its structural change. The scattered electrons would pass through a thin slit located between the specimen and the deflection plates. The slit would, in the case of the ring pattern, pass small segments of each ring and the deflection plates (with a streak direction perpendicular to the slit length) would streak the time evolution of the changing pattern. In this mode of operation the time resolution is no longer dictated by the electron burst width, but rather by the temporal resolution of the streak region in the streak tube which is at most a few picoseconds.[10] Picosecond synchronization between the laser stimulus and activation of the deflection plates would allow signal recovery techniques to be used.[5]

A further extension of the deflection mode of operation would be to replace the front end of the streak tube with a gated thermionic e-beam, thus removing the need for a photocathode. It should be possible, with an ultra-high vacuum system, to use these techniques to create a picosecond diffraction pattern in the reflection mode. This would permit investigation of surface effects on any thin or thick material.

Presently, an experiment is being carried out using the short electron pulse in transmission mode to investigate the kinetics of a material under laser annealing conditions. We believe that these techniques will make possible the investigation of laser-induced phase transitions in a time domain presently of great interest.

REFERENCES
1. R. Frankel and J. Forsyth, *Science* **204**, 622 (1979).

2. B. C. Larson, Material Research Society, Annual Meeting Boston Paper AI.2. (1981).

3. S. Williamson and G. Mourou, CLEO '81, Washington, D.C. Paper WR5 (1981).

4. D. J. Bradley and W. Sibbett, *Appl. Phys. Lett.* **27**, 382 (1975).

5. G. Mourou and W. Knox, *Appl. Phys. Lett.* **36**, 623 (1980).

6. M. C. Adams, D. J. Bradley and W. Sibbett, *Picosecond Phenomena*, edited by C. V. Shank, E. P. Ippen and S. L. Shapiro (Springer-Verlag., 1978), p. 108.

7. P. Grivet, *Electron Optics* (Pergamon Press, 1972), p. 638.

8. H. P. Klug and L. E. Alexander, *X-Ray Diffraction Procedures* (J. Wiley & Sons, 1967), pp. 319-389.

9. W. Knox (private communication).

10. H. Niu and W. Sibbett, *Rev. Sci. Instrum.* **52**, 1830 (1981).

# 4.B Generation of Pulses Shorter than 70 fsec with a Synchronously Pumped CW Dye Laser

Recently, Fork et al.[1] have reported on the generation of stable 90 fsec ($10^{-15}$ seconds) pulses, by colliding pulse mode-locking with a CW pumped passively mode-locked dye laser. At LLE we have succeeded in generating laser pulses less than 70 fsec in duration with a synchronously pumped dye laser using a solution of rhodamine 6G and DQOCI in ethylene glycol. The spectral width of these laser pulses, larger than 100 Å, suggests a frequency chirp in the pulses or a limitation in our abilty to measure the real pulse width due to a restricted phase matching bandwidth and the converging beam geometry of our background-free autocorrelator. Minimum pulse widths are obtained at 615 nm when the laser reaches its optimum output power with an overall efficiency of 10%. The laser is somewhat tunable over a 590-615 nm range with an increase in pulse width. Unlike regular synchronously pumped dye lasers, no satellite pulses or coherence spikes are observed. Furthermore, because of the excellent synchronization of the short pulse with the pump pulses, this pulse can readily be amplified by a synchronously pumped dye amplifier system.[2]

A frequency doubled CW modelocked Nd:YAG laser is used to synchronously pump a four mirror-dye laser as shown in Fig. 21. A Z-cavity configuration was used to make provision for two outputs and was not essential for the generation of short pulses. A 200 µm thick jet is used with 5 cm focal length folding mirrors. It is noteworthy that the jet does not occupy any strategic position in the cavity. The dye laser is a mixture of $5 \times 10^4$M rhodamine 6G and $3 \times 10^5$M DQOCI. An output power of 30mW is obtained for 300mW pump power. A 2 µm thick uncoated pellicle tunes the laser wavelength without restricting the laser bandwidth. The pulse width measurements are performed using a background-free autocorrelator and the integrated laser spectrum is monitored with a 1/4
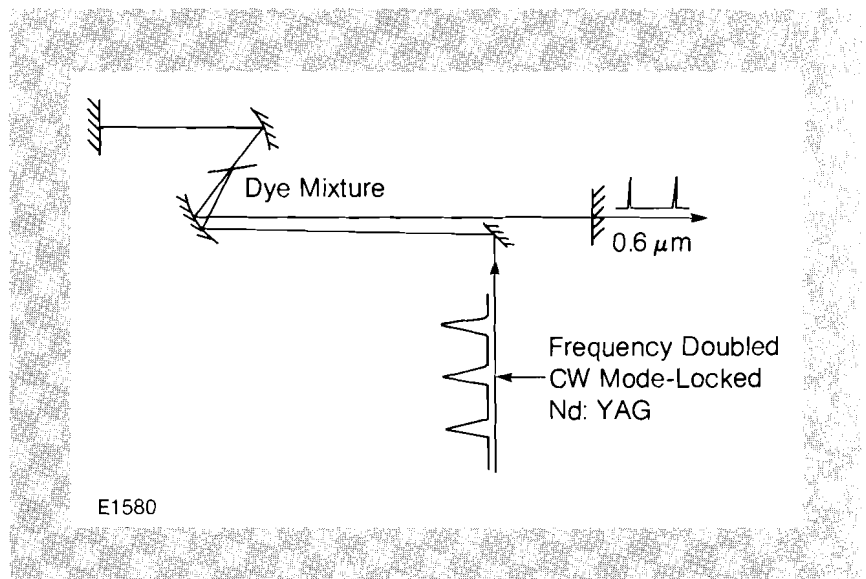


Fig. 21
Experimental set-up: a frequency-doubled CW mode-locked Nd:YAG laser pumps a dye mixture of rhodamine 6G and DQOCl in ethylene glycol in a 4-mirror cavity.

Dye Mixture

0.6 µm

Frequency Doubled CW Mode-Locked Nd: YAG

E1580

meter monochromator on an optical multichannel analyzer. Minimum pulse widths are achieved at 615 nm when the dye laser cavity length is carefully tuned to the length of the Nd:YAG laser cavity. To minimize the cavity length fluctuation, the two lasers are mounted on super invar slabs. The DQOCI[3] dye in ethylene glycol is remarkably well suited as a saturable absorber because its absorption band matches the rhodamine 6G emission band, leading to a large intensity discrimination and maximum wavelength tuning range. The dye lifetime has also been measured to be very short. Time-delay fluorimetry using a jitter-free streak[4] camera has shown that the DQOCI 1/e fluorescence time is equal to or less than 3 psec. When DQOCI is replaced by DODCI, longer pulses, around 200 fsec, are observed.

Figure 22 shows a typical autocorrelation trace suggesting a real pulse width of slightly less than 70 fsec for a hyperbolic secant pulse, which corresponds to a laser spectrum of 60 Å FWHM. The integrated spectral width is over 120 Å and suggests a restricted correlator bandwidth or a frequency chirp. This issue should be resolved with the use of KDP crystals less than 100 $\mu$m in thickness, working at a low convergence angle. The nonlinear crystal used presently in this work is 1 mm thick and exhibits a crossover length of 100 $\mu$m for converging beams. In addition to the crystal thickness which introduces a temporal broadening due to the phase matching bandwidth of the nonlinear crystal, a large waist size could lead to a significant temporal spread. For instance, a beam size of 50 $\mu$m at a 10 degree angle of convergence on the crystal, leads to a temporal spread of 30 fsec.
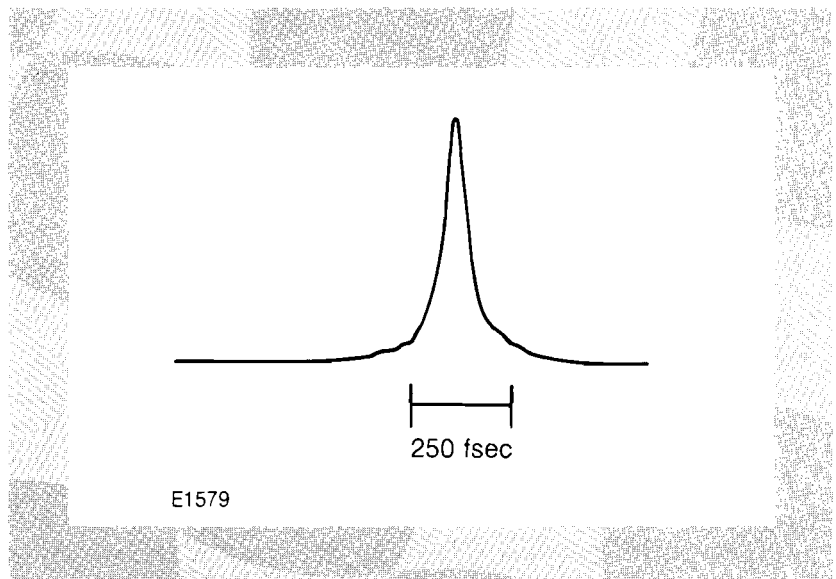


250 fsec

E1579

*Fig. 22*
*Autocorrelation trace of the optical pulse.*
*The scale has been established assuming*
*a hyperbolic secant pulse.*

In a test through dispersive media such as BK7 glass, we found that pulses starting from a different initial pulse width can be stretched or compressed according to the central frequency of the laser, suggesting a negative or positive frequency chirp across the frequency tuning range. The frequency chirp variation could stem from the interplay between the normal and anomalous dispersions in the solvent, rhodamine 6G, and DQOCI dye mixture. At frequencies corresponding to the minimum pulse width the use of dispersive glass stretches the optical pulse

and seems to indicate a positive frequency chirp. The use of a grating pair outside the cavity, in an arrangement demonstrated by Treacy,[5] should help to compress the laser pulse width towards its Fourier transform limit of 30 fsec. Also, dispersion-free cavities could be built with a judicious choice of auxiliary dye molecules or metal vapors[6] working near their absorption line.

In conclusion, less than 70 fsec pulses have been generated with a synchronously pumped dye laser using a mixture of rhodamine 6G and DQOCl. The laser exhibits maximum stability and a maximum output power at minimum pulse width, reflecting the dramatic effect of the saturable absorber. The large laser spectrum and evidence of frequency chirp indicate that shorter pulses could be obtained in a dispersion-free cavity. The availability of this system at LLE will enable researchers to investigate physical processes occurring in a variety of material and biological systems in the 0.1 psec to 1.0 psec time domain.

REFERENCES
1. R. L. Fork, B. I. Greene and C. V. Shank, *Appl. Phys. Lett.* **38**, 671 (1981).

2. T. Sizer, J. D. Kafka, A. Krisiloff and G. Mourou, *Opt. Comm.* **39**, 259 (1981).

3. D. J. Bradley in *Ultrashort Light Pulses,* edited by S. L. Shapiro, *Topics in Applied Physics* **18** (Springer-Verlag., New York, 1977), p. 57.

4. M. Stavola, G. Mourou and W. Knox, *Optics Comm.* **34**, 409 (1980).

5. E. B. Treacy, *Phys. Lett.* **28A**, 34 (1968).

6. H. Nakatsuka and D. L. Grischkowsky, *Opt. Lett.* **6**, 13 (1981).

# Section 5
# NATIONAL LASER USERS FACILITY NEWS

This report covers the activities of the National Laser Users Facility during the quarter October to December 1981. During this period most of our current users visited the Laboratory to either begin preparation for or to discuss the planning for their experiments. A total of 12 users' experiments have been approved: seven are scheduled for the OMEGA and Glass Development Laser (GDL) systems beginning in March 1982, one has been completed, one is ongoing, two are awaiting funding, and one was withdrawn.

The status of these experiments is as follows: Larry Knight (Brigham Young University) has completed his experiment, Jim Forsyth (University of Rochester) is continuing his experiment, Mark Sceats (University of Sydney, Australia) is awaiting funding for his two experiments, and Glen Dahlbacka (Physics International) has withdrawn his experiment. The remainder of our current users are in the process of fabricating the diagnostics for their respective experiments and are scheduled to begin taking data in March 1982. They include Francis Chen and Chan Joshi (UCLA) and Nizarali A. Ebrahim (Yale University), Hans Griem (University of Maryland), and Anthony Burek (National Bureau of Standards) on the GDL system; George Miley (University of Illinois), Uri Feldman and George Doschek (Naval Research Laboratory), Barukh Yaakobi (University of Rochester), and C. F. Hooper, Jr. (University of Florida) on the OMEGA system. A description of these experiments can be found in Volume 7 of the LLE Review. All of the above experiments are supported by contracts with the U.S. Department of Energy, except for Jim For-

33

syth's work, which is supported by the National Science Foundation, the National Institutes of Health, and the Air Force Office of Scientific Research.

In addition to supporting our current user experiments, we are beginning preparations for the next set of users who will be chosen by the Steering Committee during their annual meeting at LLE in late April or early May. Composed predominantly of scientists from outside the University of Rochester (see LLE Review Vol. 7 for a list of current members), the Steering Committee reviews and approves research proposals submitted to the NLUF by potential users. We have received two formal proposals and are expecting an additional sixteen. These proposals address problems in the following scientific areas: laser fusion, fundamental plasma physics, laboratory astrophysics, diagnostic development for fusion, and nuclear physics.

Opportunities for user experiments in a variety of scientific disciplines are available at the NLUF because of the unique high-energy density environment of high-power, focussed-laser radiation. This high-energy density is obtained by focusing pulsed terawatt laser beams to a spot 50 microns in diameter. Energy densities as high as $10^8 J/cm^3$, field strengths of $10^{10} V/cm$, and temperatures of over 50,000,000 °K are attainable at particle densities of $10^{23}/cm^3$. The dense, hot material so created can be an extremely intense emitter of x-rays, neutrons, and charged particles from a point source.

The NLUF offers to the user potential experiments in either laser-matter interaction or the use of x-rays or neutrons for probing the structure of matter. Laser-matter interaction experiments have yielded conditions similar to those in white dwarf stars with applications in fusion, laboratory astrophysics, and diagnostics development. X-rays or neutrons derived from these experiments permit structure analysis on the atomic and molecular scale. The x-rays emitted in this environment have been used to record biological changes in less than a billionth of a second.

Members of the Laboratory staff are available to help users in the design, construction and implementation of experiments on the OMEGA and GDL laser systems. Staff members also provide technical assistance in matching user equipment needs with in-house facility instrumentation systems. Operation of the laser is performed by Laboratory staff.

Further information on the NLUF is available from:

> Dr. Thomas C. Bristow, Manager
> National Laser Users Facility
> Laboratory for Laser Energetics
> University of Rochester
> 250 East River Road
> Rochester, New York 14623

# PUBLICATIONS AND CONFERENCE PRESENTATIONS

## Publications

B. Yaakobi, T. Boehly, P. Bourke, Y. Conturie, R. S. Craxton, J. Delettrez, J. M. Forsyth, R. D. Frankel, L. M. Goldman, R. L. McCrory, M. C. Richardson, W. Seka, D. Shvarts and J. M. Soures, "Characteristics of Target Interaction with High Power UV Laser Radiation," *Opt. Comm.* **39**, 175-179 (1981).

M. A. True, J. R. Albritton and E. A. Williams, "Fast Ion Production by Suprathermal Electrons in Laser Fusion Plasmas," *Phys. Fluids* **24**, 1885-1893 (1981).

T. M. Nordlund and W. H. Knox, "Lifetime of Fluorescence from Light-Harvesting Chlorophyll a/b Proteins," *Biophys. J.* **36**, 193-201 (1981).

T. C. Bristow, R. S. Craxton, J. Delettrez, A. Entenberg, J. Forsyth, W. Friedman, L. Goldman, F. Kalk, S. Letzring, M. Lubin, R. L. McCrory, J. Rizzo, W. Seka, S. Skupsky, J. M. Soures, E. Thorsos, C. P. Verdon and B. Yaakobi, "Symmetrically Illuminated Laser Fusion Implosion Experiments at the Laboratory for Laser Energetics," *Plasma Physics and Controlled Nuclear Fusion Research 1980,* **2,** 25-30 (1981).

T. Sizer, J. D. Kafka, A. Krisiloff and G. Mourou, "Generation and Amplification of Sub-Picosecond Pulses Using a Frequency Doubled Neodymium YAG Pumping Source," *Opt. Comm.* **39,** 259-262 (1981).

Y. Conturie, B. Yaakobi, U. Feldman, G. A. Doschek and R. D. Cowan, "Observation of New Lines of Xe XLIV, XLV, XLVI, and XLVII in the Range 2.5-3.0 Å from Laser-Imploded Targets," *J. Opt. Soc. Am.* **71,** 1309-1314 (1981).

J. A. Abate, "Flashlamp-Induced Thermal Distortion in an Active-Mirror Nd:Glass Laser Amplifier," *SPIE Vol. 293 Wavefront Distortions in Power Optics,* 114-125 (1981).

G. Albrecht, A. Antonetti and G. Mourou, "Temporal Shape Analysis of $Nd^{3+}$:YAG Active Passive Mode-Locked Pulses," *Opt. Comm.* **40,** 59-61 (1981).

R. E. Hopkins, "Geometrical Optics in a Laser Laboratory," *SPIE Vol. 288 Los Alamos Conference on Optics,* 568-579 (1981).

# Forthcoming Publications

W. Seka, R. S. Craxton, J. Delettrez, L. Goldman, R. Keck, R. L. McCrory, D. Shvarts, J. M. Soures and R. Boni, "Measurements and Interpretation of the Absorption of 0.35$\mu$m Laser Radiation on Planar Targets," accepted by *Optics Communications.*

D. H. Berwald and J. A. Maniscalco, "Performance and Economic Analysis of Several Laser Fusion Breeder Fueled Electricity Generation Systems," accepted by *Nuclear Technology/Fusion.*

M. Chou and G. A. Zawadzkas, "Long-Pulse $N_2$ UV Lasers at 357.7, 380.5, and 405.9 nm in $N_2$/Ar/Ne/He Mixture," accepted by *IEEE Journal of Quantum Electronics.*

G. A. Mourou and T. Sizer, "Generation of Pulses Shorter than 70 fs with a Synchronously-Pumped CW Dye Laser," accepted by *Optics Communications.*

# Conference Presentations

Y. Conturie, "Soft X-Ray Population Inversion from Aluminum Targets Irradiated by a Frequency-Tripled Nd:Glass Laser," presented at the Annual Meeting of the Optical Society of America, Kissimmee, Florida, October 1981.

R. Bingham, R. Short and E. Williams, "Modulational Instability of a Standing Electromagnetic Wave," presented at the Annual Meeting of the APS Division of Plasma Physics, October 1981.

T. Boehly, L. M. Goldman, M. C. Richardson. W. Seka, J. M. Soures and R. S. Craxton, "Ion Blow-Off Measurements of 0.35 $\mu$m Laser Plasmas," presented at the Annual Meeting of the APS Division of Plasma Physics, October 1981.

T. Bristow, B. Brinker, J. Boles, A. Entenberg, R. Hutchison, L. Iwan, S. Letzring, S. Kacenjar, R. Nimick, R. Peck, W. Seka, J. M. Soures, D. Villeneuve, B. Yaakobi and M. C. Richardson, "Initial Target Experiments with OMEGA," presented at the Annual Meeting of the APS Division of Plasma Physics, October 1981.

R. S. Craxton, J. Delettrez, R. L. McCrory, D. Shvarts, T. Boehly, R. Keck,

W. Seka and B. Yaakobi, "Simulations of Short Wavelength Laser-Plasma Interaction Experiments," presented at the Annual Meeting of the APS Division of Plasma Physics, October 1981.

J. Delettrez and S. Skupsky, "Target Designs for the 0.35 $\mu$m Implosion Experiments on the OMEGA Laser System," presented at the Annual Meeting of the APS Division of Plasma Physics, October 1981.

R. Epstein, D. Shvarts, J. Delettrez, R. L. McCrory and C. P. Verdon, "Self-Consistent Flux Limitation of Transport Coefficients in Hot Plasmas," presented at the Annual Meeting of the APS Division of Plasma Physics, October 1981.

W. D. Friedman, S. Kumpan, D. Villeneuve, J. Hoose and R. Hopkins, "Laser Beam Characterization Experiments on the OMEGA Facility," presented at the Annual Meeting of the APS Division of Plasma Physics, October 1981.

L. M. Goldman, M. C. Richardson, W. Seka, K. Tanaka, R. Bingham and E. Williams, "Raman Backscattering from UV Laser-Produced Plasmas," presented at the Annual Meeting of the APS Division of Plasma Physics, October 1981.

S. Kacenjar, L. M. Goldman, A. Entenberg, and S. Skupsky, "Measurement of Fuel $\rho$R in Laser Fusion Using CR-39 Solid-State Track Detectors," presented at the Annual Meeting of the APS Division of Plasma Physics, October 1981.

R. L. Keck, R. S. Craxton, L. M. Goldman, W. Seka and J. M. Soures, "Continuum X-Ray Measurements of Laser Plasmas Generated by 0.35 $\mu$m Irradiation," presented at the Annual Meeting of the APS Division of Plasma Physics, October 1981.

K. K. Lee, R. Hopkins and R. L. McCrory, "Uniformity of Illumination on Spherical Targets," presented at the Annual Meeting of the APS Division of Plasma Physics, October 1981.

S. Letzring, B. Brinker, A. Entenberg, R. Hutchison, L. Iwan, R. Nimick, R. Peck, M. C. Richardson, J. M. Soures, D. Villeneuve, J. Delettrez and D. Shvarts, "Irradiation Geometry Studies with Multiple Beams," presented at the Annual Meeting of the APS Division of Plasma Physics, October 1981.

R. S. Marjoribanks, M. C. Richardson, J. Delettrez, S. Letzring, W. Seka and D. Villeneuve, "Time-Resolved X-Ray Spectrometry from UV Laser-Produced Plasmas," presented at the Annual Meeting of the APS Division of Plasma Physics, October 1981.

R. L. McCrory and D. Shvarts, "A Hybrid Model for Thermal Electron Transport Simulation for Laser Fusion Plasmas," presented at the Annual Meeting of the APS Division of Plasma Physics, October 1981.

M. C. Richardson, L. M. Goldman, W. Seka, J. M. Soures, K. Tanaka, R. Bingham and E. Williams, "Raman Side-Scattering and Evidence of $2\omega_p$ Instability in UV Laser Plasmas," presented at the Annual Meeting of the APS Division of Plasma Physics, October 1981.

W. Seka, L. M. Goldman, J. Hoose, M. C. Richardson, J. M. Soures, B. Yaakobi, D. Villeneuve, T. Boehly, R. Keck, K. Tanaka, R. Boni, R. S.

Craxton, J. Delettrez, R. L. McCrory and D. Shvarts, "Laser-Plasma Interaction Experiments as 0.35 $\mu$m," presented at the Annual Meeting of the APS Division of Plasma Physics, October 1981.

R. W. Short, R. Bingham and E. A. Williams, "Filamentation Instability in Flowing Plasma," presented at the Annual Meeting of the APS Division of Plasma Physics, October 1981.

D. Shvarts, R. S. Craxton, J. Delettrez, R. L. McCrory, C. P. Verdon and B. Yaakobi, "Analysis of Thermal Transport Inhibition in Intense Laser-Plasma Interactions," presented at the Annual Meeting of the APS Division of Plasma Physics, October 1981.

S. Skupsky, "Charge-Particle Energy Loss in High-Z High-Density Matter," presented at the Annual Meeting of the APS Division of Plasma Physics, October 1981.

J. M. Soures, L. M. Goldman, M. C. Richardson, W. Seka, K. Tanaka, R. Bingham and E. Williams, "Experimental Evidence of Parametric Instabilities in Laser Plasmas," presented at the Annual Meeting of the APS Division of Plasma Physics, October 1981.

K. Tanaka, L. M. Goldman, W. Seka, R. Bingham, R. Short and E. Williams, "Time-Resolved Backscatter Spectra Around $\omega_0$ from 0.35 $\mu$m Laser Plasmas," presented at the Annual Meeting of the APS Division of Plasma Physics, October 1981.

C. P. Verdon, R. L. McCrory and D. Shvarts, "Effects of Pusher-Fuel Interface Unstable Growth on Ignition of 'Levitated Fuel' Inertial Confinement Fusion Targets," presented at the Annual Meeting of the APS Division of Plasma Physics, October 1981.

D. Villeneuve, M. C. Richardson, W. Seka, R. Bingham, R. Short and E. Williams, "Filamentation in Short Wavelength Laser Plasmas," presented at the Annual Meeting of the APS Division of Plasma Physics, October 1981.

B. Yaakobi, T. Boehly, Y. Conturie, R. S. Craxton, J. Delettrez, J. M. Forsyth, R. D. Frankel, L. M. Goldman, R. L. McCrory, W. Seka and J. M. Soures, "Characteristics of Target Interaction with a Frequency Tripled Nd:Glass Laser of Power 0.1-0.2 TW," presented at the Annual Meeting of the APS Division of Plasma Physics, October 1981.

B. Yaakobi, T. Boehly, Y. Conturie, R. S. Craxton, J. Delettrez, J. M. Forsyth, R. D. Frankel, L. M. Goldman, R. L. McCrory, W. Seka and J. M. Soures, "Preheat Measurements in UV-Laser Target Interaction," presented at the Annual Meeting of the APS Division of Plasma Physics, October 1981.

B. A. Brinker and J. R. Miller, "Fabrication of Inertial Fusion Targets with Fill Support Capillaries," presented at the American Vacuum Society Meeting, November 1981.

D. Glocker and R. Wiseman, "A New Method for the Batch Production for Micro-Fresnel Zone Plates," presented at the American Vacuum Society Meeting, November 1981.

D. Glocker, J. Drumheller, and J. R. Miller, "Ion Beam Sputter Deposition onto Levitated and Stalk Mounted Laser Fusion Targets," pre-

sented at the American Vacuum Society Meeting, November 1981.

I. S. Goldstein, J. Varon and P. J. McHugh, "RF vs DC Sputter Gun Copper Coating of Laser Fusion Targets," presented at the American Vacuum Society Meeting, November 1981.

H. Kim, J. Mason, J. R. Miller, M. Mehicic and J. Lippert, "Improved Inertial Fusion Target Ablation Layer Fabrication Using Alkyl Substituted Di-Para-Xylylenes," presented at the American Vacuum Society Meeting, November 1981.

T. F. Powers, "Improved Nonconcentricity Characterization of Transparent Laser Fusion Targets by Interferometry," presented at the American Vacuum Society Meeting, November 1981.

Y. Conturie, J. Delettrez, B. Yaakobi and J. Forsyth, "Soft X-Ray Population Inversions in Laser-Produced Plasmas," presented at the 46th Statistical Mechanics Meeting, Rutgers, December 1981.